Evaluating Microphysical Parameterization Schemes for Use in Hurricane Environments. Part I: Comparisons with observations

Robert Rogers[1], Michael Black[1], Shuyi Chen[2] and Robert Black[1]

[1]NOAA/AOML Hurricane Research Division
4301 Rickenbacker Causeway
Miami, FL 33149

[2]Department of Meteorology and Physical Oceanography
Rosenstiel School for Marine and Atmospheric Science
University of Miami
Miami, FL 33149

Submitted to *Journal of the Atmospheric Sciences*
as a part of the CAMEX Special Issue

23 December 2003

Abstract

In this study a commonly used and relatively sophisticated microphysical parameterization scheme used in high-resolution tropical cyclone simulations is compared to airborne radar and microphysical probe data collected from storms over many years, including as a part of the NASA Third Convection and Moisture Experiment (CAMEX III). Statistics of vertical motion, reflectivity, and hydrometeor concentrations are compared for the two datasets (observations versus simulations) to identify possible deficiencies in the microphysical scheme and areas for improvement to the scheme. Such improvements can potentially lead to better forecasts of tropical cyclone intensity and rainfall.

Comparisons of the two populations show that the model reproduces many of the gross features seen in the observations, though notable differences are evident. The general distribution of vertical motion is similar between the observations and simulations, with the strongest up- and downdrafts comprising a small percentage of the overall population in both datasets, but the magnitudes of vertical motion are weaker in the simulations. The model produces reflectivities that are much larger than observed, and correlations between vertical motion and hydrometeor concentration and reflectivity show a much stronger relationship in the model than what is observed.

These comparisons show that there are several areas of deficiency that may reflect problems with the parameterization, such as with the production, conversion, and fallout of frozen hydrometeors. Future investigations will test proposed changes in the parameterizations of these processes with the goal of improving the statistics in the simulations. The comparison technique presented here provides a reliable method for testing simulations against observations, and it provides a framework for conducting comparisons using other observational platforms.

1. Introduction

There are many factors that determine a tropical cyclone's intensity and rainfall, such as the magnitude and direction of vertical shear affecting the storm core, upper oceanic temperature structure, and low- and mid-level environmental relative humidity. Ultimately, though, intensity and rainfall are dependent on the magnitude and distribution of the release of latent heat within the core of the storm (Willoughby 1995). Despite the recognition of this importance, improving our understanding and forecasting of intensity and rainfall remains an elusive goal for the operational and research communities, as evidenced by the fact that forecasts of intensity have shown virtually no improvement over the past 20 years. Furthermore, the importance of improving tropical cyclone rainfall forecasts is underscored by the fact that drowning due to inland flooding from tropical cyclones is the leading killer from landfalling storm in the United States over the past 30 years (Rappaport 2000).

High-resolution (grid length $\approx$ 1 km) numerical models have been used as a tool to investigate the processes important in determining tropical cyclone intensity and rainfall. Such high resolution obviates the need for the parameterization of deep convection, a traditional source of uncertainty in determining latent heating profiles. While convective parameterization is avoided using high resolution, the parameterization of microphysical processes such as hydrometeor production, conversion, and fallout, is still necessary at this resolution. The dependence of these microphysical processes on the rainwater, ice and graupel distributions thus assumes great importance in determining latent heating distributions and, ultimately, tropical cyclone intensity and rainfall.

As a result of this sensitivity to the microphysical processes, the success of numerical simulations of tropical cyclones is, to some extent, dependent on how these processes are parameterized in the model. Such parameterizations range in complexity from a simple removal of supersaturation to spectral ice schemes that explicitly predict the size spectra of ice particles (Hall 1980; Farley and Orville 1986). Most schemes used in mesoscale and cloud-scale models today are bulk microphysical schemes that use two or three categories to describe the presence of ice. They are called "bulk" schemes because they assume a time-invariant size distribution for each species in the scheme. Schemes with two ice categories, called two-class ice schemes, have separate prognostic

equations for cloud ice and precipitating ice, usually taken to be snow (Cotton et al. 1982; Hsie et al. 1984). More sophisticated three-class ice schemes have prognostic equations for cloud ice, snow, and a third class of ice that is formulated to be either hail (Lin et al. 1983) or graupel (Rutledge and Hobbs 1984). A four-class ice scheme has also been formulated (Ferrier 1994) that has separate equations for cloud ice, snow, graupel, and hail. The benefit of this scheme is that it is applicable to a wide range of environments, from mid-latitude continental convection to tropical squall lines (Ferrier et al. 1995).

The sensitivity of simulations of deep convection to the type of microphysical scheme used has been shown by a number of studies. Using the fourth-generation Penn State/NCAR hydrostatic mesoscale model MM4, Zhang (1989) investigated the sensitivity of simulations of a midlatitude mesoscale convective system and associated mid-level mesoscale vortex using parameterizations using no ice phase and using a two-class ice scheme. He found that freezing and deposition in the upper levels were important processes in causing the rapid development of the mid-tropospheric warm core vortex, while subcloud-layer melting weakened the concentration of cyclonic vorticity in the lower levels. McCumber et al. (1991) used a NASA three-dimensional non-hydrostatic cloud model to compare simulations using no ice scheme, a two-class ice scheme, and a three-class ice scheme. They found that three-class ice schemes produced better results than two-class ice schemes, with the optimal mix of bulk ice hydrometeors for tropical convection being cloud ice, snow, and graupel. In a simulation of an idealized tropical cyclone using an axisymmetric, nonhydrostatic model, Lord et al. (1984) found that inclusion of a three-class ice scheme produced significant differences in the structure and evolution of the simulated storm when compared with a run with no ice. The simulation with ice processes had a much slower intensification rate initially, though it eventually reached an intensity higher than the run with no ice. Further, the simulation with ice processes had much more detailed mesoscale structure than the no-ice run, with pronounced mesoscale downdrafts forming below the melting level. These downdrafts caused low-level convergence that triggered the formation of banded features outside the eyewall, similar to those observed by Willoughby et al. (1984).

With the advent of more computing power, high-resolution, nonhydrostatic, three-dimensional models of tropical cyclones have become more widely used. Researchers have conducted simulations

of Hurricanes Andrew of 1992 (Liu et al. 1997; Zhang et al. 2000), Bob of 1991 (Braun et al. 1999), Bonnie of 1998 (Rogers et al. 2003), and Floyd of 1999 (Tenerelli and Chen 2002) using the fifth-generation Penn State/NCAR nonhydrostatic mesoscale model MM5, with structures similar to those observed. These simulations use either two- or three-class ice microphysics schemes. A commonly seen bias in high-resolution tropical cyclone simulations is the tendency of simulations to produce reflectivities that are too large when compared with airborne and ground-based radar images (e.g., Liu et al. 1997, Rogers et al. 2003). An example of this bias is shown in Figure 1, which shows a comparison of a lower fuselage (LF) WP-3D radar sweep from Hurricane Floyd taken at 22:59 UTC 13 September 1999 with reflectivity produced by a 1.67-km MM5 simulation of Hurricane Floyd from 23:00 UTC 13 September 1999. Both the LF radar sweep and the simulation indicate a nearly closed eyewall and multiple rainbands extending out from the southeastern side of the storm. However, the model produces reflectivities that are much larger in both the eyewall and the rainband regions than the radar composite. Maximum reflectivities from the radar are 33 dBZ in isolated locations, with very tiny patches of reflectivity greater than 39 dBZ evident in the eyewall. In contrast, the entire eyewall and numerous portions of the rainbands in the Floyd simulation are enclosed by a 41 dBZ contour, and many locations within the eyewall and rainbands exceed 48 dBZ.

Many studies have been performed to investigate the structure of tropical cyclones from radar and microphysical measurements (e.g., Marks and Houze 1987; Black and Hallett 1986; Black 1990; Black et al. 1996). Very little work has been done, however, in performing detailed, rigorous comparisons between models and these observational datasets. In this study high-resolution simulations of Hurricanes Bonnie (Rogers et al. 2003) and Floyd (Tenerelli and Chen 2002) are compared with observations from nine different storms in order to evaluate the ability of the models to reproduce the statistics of the distributions of vertical motion, reflectivity, and hydrometeor mixing ratio seen in the data. The observations used in the intercomparisons are tail-mounted vertical incidence Doppler radar data (to provide vertical motion and reflectivity), microphysics probe data (to provide hydrometeor concentrations), and flight-level data (to provide vertical motion at flight level). Since convective processes occur on very small temporal and spatial scales, it is quite difficult to have

model output and observations at precisely the same location, and at the same time, in the life cycle of any such small-scale feature. The technique of comparing the statistical properties (e.g., means, standard deviations, probability distribution functions, and correlations) of the distribution of relevant parameters in both the models and the observations reduces the need for a precise temporal and spatial match, and it allows for a more comprehensive and robust evaluation of the microphysical parameterization scheme to be performed. This study provides a comprehensive comparison between high-resolution simulations of tropical cyclones and observations from a variety of storms, in order to provide a more robust measure of the performance of the microphysical scheme in the model and identify possible areas for improvement.

In this paper section 2 provides a description of the methodology employed in the comparisons, including a summary of the model parameters and data analysis techniques. Section 3 presents the results from the comparisons, and section 4 discusses the implications of the results of these comparisons for the microphysical parameterization scheme used here. Section 5 provides concluding remarks.

2. Methodology

a) Model description

(1) MODEL CONFIGURATIONS AND SIMULATIONS

The numerical model used in this study was the fifth generation Penn State University/NCAR nonhydrostatic mesoscale model (MM5, Grell et al., 1994). The MM5 is a fully nonlinear, nonhydrostatic mesoscale model that has a well-demonstrated ability to simulate tropical cyclones (e.g., Liu et al., 1997; Karyampudi et al., 1998; Braun and Tao 2000; Braun 2002; Rogers et al. 2003; Tenerelli and Chen 2002). A detailed description of the model equations and coordinates is given by Grell et al. (1994). Briefly, the model uses a reference-state pressure to define a σ-coordinate. The perturbation from this reference state is then the predicted variable rather than the full pressure. The model variables are pressure perturbation, horizontal and vertical wind components, temperature,

specific humidity, and depending on the choice of microphysical parameterization scheme, cloud water, cloud ice, rainwater, snow, and graupel.

A unique aspect of these simulations is the use of a vortex-following nested-grid that allows for long integrations with very high grid resolution in the inner core region of hurricanes (Tenerelli and Chen 2004). The simulations presented here use four domains, with grid lengths of 45, 15, 5, and 1.67 km. The inner domains move automatically with the storm, with the location of the domain based on the location of the 500 hPa geopotential minimum associated with the storm. High-resolution (30 second) terrain and land-use data are used in the simulations. Because the location of the inner meshes are not known in advance of running the simulations, it is not possible to generate in advance high-resolution terrain and land-use files for each of the mesh locations. Therefore the model was modified so that elevation and land use data are read and placed on the fine meshes each time they are initialized or moved. There are 28 vertical levels in the model, with vertical resolution maximized in the lowest 100 hPa (roughly 50 m spacing) and the spacing between levels increasing with increasing height (up to a maximum spacing of about 900 m).

The model initial and lateral boundary conditions for the outer-most domain during integration are from the National Center for Environmental Prediction Aviation (AVN, now the Global Forecasting System) model one-degree analysis fields. Sea-surface temperatures are enhanced by incorporating 9-km AVHRR Pathfinder SST into the SST field. For the two outer meshes (45 and 15 km), the Kain-Fritsch convective parameterization scheme is used (Kain and Fritsch 1993). This scheme includes a relatively sophisticated cloud model that determines entrainment and detrainment rates as a function of the local environment and includes the effects of downdrafts. Modifications to the Kain-Fritsch scheme include the detrainment of 30% of hydrometeors to the resolvable grid and a higher vertical velocity threshold for the initiation of convective clouds, which is more suitable for tropical oceanic conditions. On the inner two meshes, the deepest and strongest convective towers are explicitly resolved, so no convective parameterization scheme is used for those meshes. The Blackadar boundary layer parameterization scheme, which simulates the vertical mixing of temperature, water vapor, momentum, and cloud water, is used on all meshes (Zhang and Anthes

1982), and a simple radiation scheme that allows for the impact of clouds on shortwave and longwave radiation is used (Dudhia 1989). The Blackadar scheme is modified for these runs to include the modification based on Pagowski and Moore (2001) in which different roughness scales for temperature z_t and moisture z_q are used. This configuration of the model has been used successfully to simulate Hurricane Bonnie of 1998 (Rogers et al. 2003), Hurricane Georges of 1998 (Orndorff et al. 2002), and Hurricane Floyd of 1999 (Tenerelli and Chen 2002).

For the comparisons presented here, high-resolution multi-day simulations of Hurricanes Bonnie and Floyd are used. Hurricane Bonnie was a storm that encountered significant shear for parts of its lifetime, limiting its development to a Category 2 with a minimum central pressure of 954 hPa in the western Atlantic (Pasch et al. 2001, Rogers et al. 2003). Hurricane Floyd experienced a favorable environment for intensification and nearly reached Category 5 strength over the warm waters just northeast of the Caribbean Sea (Lawrence et al. 2001). The simulation of Hurricane Bonnie is a five-day simulation, with the highest-resolution 1.67-km domain used for the final two days of the simulation. The simulation of Hurricane Floyd is a seven-day simulation, with the 1.67-km domain used for the final 4.5 days of the simulation. These simulations reproduced the track and intensity of both storms reasonably well (Fig. 2). Hourly output during a 24-h period for each simulation was used to generate the database with which to perform the comparison with observations. The 24-h time period chosen in each simulation was the time when the simulated intensity was closest to the observed intensity and the simulated storm was in approximate steady state.

(2) MICROPHYSICAL PARAMETERIZATION SCHEME

The microphysical parameterization scheme used in these simulations is the Tao-Simpson (Tao and Simpson 1993) cloud microphysics scheme for all four meshes. The Tao-Simpson scheme, which was modified from Lin et al. (1983), is a bulk three-class ice scheme that contains prognostic equations for cloud water (ice), rainwater (snow), and hail/graupel, and it allows for the generation of supercooled water. This scheme includes the processes of condensation/evaporation, freezing/melting, sublimation/deposition, autoconversion (i.e., aggregation) of cloud water (ice, snow) to form rainwater (snow, hail/graupel), collection by rainwater (snow), and accretion.

Nonprecipitating particles (i.e., cloud water and ice) are assumed to have monodisperse distributions, while all other particles are assumed to have Marshall-Palmer type distributions (Marshall and Palmer, 1948):

$$N(D) = N_0 e^{-\lambda D} dD \tag{1}$$

where N = number of particles for a given diameter range
D = diameter of particles (m)
N_0 = intercept parameter (m^{-4})
λ = slope parameter (m^{-1})

Values of the intercept and slope parameters are predefined, and they are dependent on the species, with the largest values of the intercept parameter associated with rain and the smallest associated with snow. Precipitation fall speeds (V_m) in the scheme are calculated by:

$$V_m = \frac{\int V(D) m(D) N(D) dD}{\int m(D) N(D) dD} \tag{2}$$

where V(D) is the terminal velocity of an individual particle (parameterized empirically from observations), m(D) represents the hydrometeor mass, and N(D) is the number density (defined by Eq. 1). Reflectivity in the model is calculated using the total mass content of individual constituent species and adding their reflectivity values together to yield a total reflectivity value (Braun and Houze 1994, Fovell and Ogura 1988):

$$Z_e = 720 \alpha \kappa N_{0x} \left(\frac{\rho_x}{\rho_w} \right)^2 \left[(\pi \rho_x N_{0x} / \rho q_x)^{1/4} \right]^{-7} \tag{3}$$

where Z_e = equivalent reflectivity (mm^6)
α = ratio of backscattering coefficients for the reflecting particles and water (taken as 1 for rain and 0.213 for precipitating ice)
κ = conversion factor from m^3 to $mm^6 m^{-3}$ (equal to 10^{18})
ρ_x = density of particle (kg m^{-3}; frozen or liquid depending on type of particle being considered)
ρ_w = density of water (kg m^{-3})
ρ = density of air (kg m^{-3})
q_x = mixing ratio of species x (i.e., rain, snow, graupel; kg kg^{-1})

Equation (3) can be rewritten as

$$Z_e = \kappa C\,(\rho q_x)^{1.75} \tag{4}$$

Where

$$C = \frac{720\alpha N_{0x}}{\left(\pi\rho_x N_{0x}\right)^{1.75}}\left(\frac{\rho_x}{\rho_w}\right)^2 \tag{5}$$

From this relationship it can be seen that the reflectivity calculated in the model is dependent on the assumed intercept parameter (N_0), assumed particle density (ρ_x), and simulated mixing ratio (q_x) for each species.

b) Description of observing platforms

(1) VERTICAL INCIDENCE (VI) RADAR

Vertical motions are calculated using data recorded from Doppler radar systems on each of the two NOAA WP-3D research aircraft. The 3.2-cm Doppler radar is mounted on the tail of the aircraft and scans in a vertical plane normal to the aircraft track. The radar system records reflectivity data that describe the precipitation structure in a vertical plane along the flight track and radial velocities of precipitation particles, toward and away from the aircraft. When the antenna is at vertical incidence (VI), the Doppler velocities are the vertical motions of precipitation particles relative to the aircraft.

The WP-3D flies at typical ground speeds of ~125 m s^{-1}, so that VI Doppler data are available at intervals of ~750 m along the flight track. In the horizontal, the radial leg lengths (penetrations into or exits out of the eye) vary from 60 to 125 km in length, depending on the flight pattern flown for a particular research mission. In the vertical, the VI data are averaged in 300 m intervals (bins) that extend from just above the sea surface to a height of 15 km. To calculate the vertical winds, the hydrometeor fallspeeds and the vertical motions of the aircraft are removed from the raw Doppler radial velocities. The particle fallspeeds are determined with bulk formulae using radar reflectivity as a function of height. The aircraft motions are calculated using a combination of inertial navigation equipment and radar altimetry. These procedures follow the methodology of Black et al. (1996), in which a subset of the VI data described here were used in a statistical study of vertical velocities and radar reflectivity. A summary of the storm names and intensities, and radial leg information for the VI

data used in this study, is in Table 1. Observations from nine storms, comprising 233 radial legs, were included in the observational database. The storms that were simulated, Hurricanes Bonnie and Floyd, were not available to be added to the VI database because the tail radar was operating in Fore/Aft Scanning Mode (F/AST)[1] during those storms.

(2) MICROPHYSICS PROBE

Particle image data from Hurricane Bonnie obtained with the NASA DC-8 aircraft were obtained with the Particle Measuring Systems (PMS) optical array probe OAP model 2D-P mono probe. This probe has a 32-element photosensitive array, measures particles of 0.2 – 6.4 mm in diameter, and has been discussed in many publications (e.g, Black and Hallett (1986)). These data were cleaned of image artifacts using the methods described by Black and Hallett (1986). The 2D-P data were averaged for 6 s. At the DC-8 airspeed of ~ 205 m/s, this corresponds to a sample length of ~1.2 km. In order to build a stable size distribution, at least 100 or more particle images must be obtained.

c) Evaluation techniques

(1) STATISTICAL COMPARISON METHODOLOGY

Despite the importance of performing rigorous comparisons between observed and model-produced microphysical properties, only a cursory comparison of gross features between modeled and observed fields has been reported in the literature. Convective processes occur on very small temporal and spatial scales, so it is quite difficult to have model output and observations at precisely the same location, and at the same time, in the life cycle of any such small-scale feature. The technique of comparing the statistical properties of the distribution of relevant parameters in both the models and the observations precludes the need for a precise temporal and spatial match, and it allows for a more comprehensive and robust evaluation of the microphysical parameterization scheme to be performed.

One method for comparing model output and observations is to create contoured frequency by altitude diagrams (CFADs; Yuter and Houze 1994). These diagrams essentially plot the variation of

[1]F/AST is a technique for deducing horizontal wind fields by having the radar antenna alternate between angles up to 20 degrees from perpendicular to the aircraft heading, so there were no radar beams at vertical incidence during those storms

probability distribution functions with height. They provide valuable information about the distributions of parameters, rather than just the means. This technique was used to study the detailed temporal evolution of vertical motion and reflectivity in a midlatitude mesoscale convective system (Yuter and Houze 1994) and the statistical properties of vertical motion and reflectivity from a multitude of tropical cyclones (Black et al. 1996).

For this study the VI observations are used to create the CFADs for comparison with the model output, since only the VI data provide the coverage in the vertical necessary to produce the CFADs. To calculate the CFADs the model output from the 1.67-km grid is interpolated to a cylindrical grid with a radial resolution of 1.67 km, an azimuthal resolution of 5 degrees, and a vertical resolution of 300 m. The VI data are interpolated to a cylindrical grid with the same azimuthal and vertical resolution, but with a radial resolution of 1.5 km. Depending on the ground speed of the aircraft, the resolution of the raw VI data is around 0.75 km, so values of reflectivity and vertical motion from adjacent measurements from the tail radar are averaged together to produce a resolution of 1.5 km. The result is a cylindrical grid with dimensions (r,λ,z) of 165x72x50, covering a region of nearly 250 km radius. Observations from the radar data normally extend out to about 150 km, so the outer radii are considered as missing data. The centers of the storms are available from flight-level data for the radar observations and are defined as the location of minimum wind speed at 1.5 km for the simulations. Each flight typically contains 5-15 radial legs, normally taken along different azimuths (azimuths are defined from north). Each of the legs within a given flight is assigned to a specific azimuth in the cylindrical grid, with the remaining azimuths assigned missing values. The result is an equivalent cylindrical grid of VI radar observations for each flight that can be processed in the same manner as the simulations.

(2) SEPARATION INTO EYEWALL, RAINBAND, AND STRATIFORM REGIONS

As a part of the comparisons, each of the radials in the cylindrical grids was divided into eyewall, rainband, and stratiform regions, as was done in Black et al. (1996). Unlike the technique in Black et al. (1996) which was based on manually evaluating reflectivity patterns from tail and lower-fuselage radar, this technique is an objective algorithm based on reflectivity and vertical motion fields.

The algorithm uses the reflectivity fields to first define candidate eyewall, rainband, and stratiform regions, and then it uses the vertical motion fields to identify the eyewall and rainband zones within each candidate region. Appendix A provides a detailed description of the classification algorithm.

Figure 3 provides examples of the sorting algorithm for two different storms: Hurricane Olivia (1994) from the VI data and the simulation of Floyd (1999). As can be seen from the figure, the scheme does a reasonably good job of differentiating among eyewall, rainband, and stratiform regions, even for storms as different as these. Statistics from the stratification of both the radar and simulation datasets are presented in Table 2. There are significantly more data points from the simulations than the observations, since the data is taken hourly over a 24-h time period at all 72 azimuths for each simulation, while only 5-15 azimuths in the observations contain data from each flight. However, the 3500 points in the radar dataset represents our best estimate of the observed statistics, and it is not felt that the discrepancy in data coverage impacts any inferences made in comparing the two datasets. For both the observations and the simulations, eyewall and stratiform regions comprise the bulk of the data. Stratiform regions comprise the majority of points (63% of all points in the observations, 48% in the simulations), while eyewall regions are the second most represented area (24% of all points in the observations, 19% in the simulations). When normalized by area, the preponderance of stratiform points was even more pronounced (69% of total area for observations and 55% for simulations). This reflects the fact that the stratiform regions are typically located radially outward of the eyewall regions, so they span a larger area per unit radial and azimuthal span. The eyewall areal coverage is 16% for the observations and 15% for the simulations, and the rainband areal coverage is 5% for the observations and 11% for the simulations.

3. Results

a) Mean profiles

Profiles of mean vertical motion and reflectivity for the observed and simulated eyewall, rainband, and stratiform regions are shown in Figure 4. The observed mean eyewall vertical motion shows relative maxima of about 2 m s^{-1} at 5 km and in the upper troposphere at 12.5 km, while a

relative minimum of about 0.3 m s^{-1} is located at about 1.5 km and another minimum of 1 m s^{-1} is located in the 6-9 km layer. This upper-level minimum, which is above the melting level, has been seen in other observations of oceanic and tropical cyclone convection (Black et al. 1996, Jorgensen et al. 1994, Jorgensen and LeMone 1989). It has been hypothesized that it is caused by water loading and entrainment effects above the melting level that reduce updraft magnitudes. The maximum in the upper troposphere is likely caused by updrafts losing their hydrometeors and reaching a maximum as water loading effects are reduced (Black et al. 1996), and the sharp drop above the maximum occurs as the eyewall updrafts encounter the tropopause. The observed rainband profile shows downward motion below 3 km followed by a sharp peak in upward motion at the melting level. The sharp spike in upward motion in the rainband region is likely attributable to uncertainties in the fall speed estimation used to derive the vertical motion, which can be as large as 2 m s^{-1} in the melting layers of convective regions (Black et al. 1996). The upward motion then decreases sharply, remaining constant with height at about 1.2 m s^{-1} up to 15 km. The magnitude of the upward motion above the melting level is comparable to that of the eyewall. The observed stratiform region shows a similar pattern to the rainband region, though the low-level vertical motion is near zero, rather than downward, and the midlevel upward motion peak is not as pronounced.

By contrast to the observed vertical motion profiles, the simulated vertical motion profiles show much less detail. The simulated eyewall vertical motion is upward throughout the entire troposphere. There is no peak in upward motion at the melting level (which is no surprise because there is no error in fall speed estimation), but the upward motion does increase steadily with increasing height, reaching a maximum of about 1 m s^{-1} at 10 km. The magnitudes of the eyewall vertical motion are slightly less than the observed upward motion, though magnitudes are comparable at 10 km. Differences between the observed and the simulated eyewall vertical motions are significant at the 99% confidence level in the 3-6 km layer and 12-13.5 km layer. The simulated rainband region has weaker vertical motion than the observed rainband region, but there is no downward motion in the lower troposphere and no upward motion spike at the melting level. The stratiform profile in the model is nearly zero from the surface up to 10 km, after which point it increases to 0.3 m s^{-1} in the

upper troposphere. Differences between the observed and simulated vertical motions are significant at the 99% confidence level over nearly the entire troposphere in the rainband and stratiform regions.

The observed mean eyewall reflectivity profile (Fig. 4b) shows a structure similar to that seen in Black et al. (1996) for the VI data. Mean reflectivity is around 35 dBZ in the lower troposphere, and it increases to a maximum greater than 40 dBZ near the melting level at 4.5 km. Above the melting layer, the reflectivity drops sharply, but then shows a secondary peak near 7.5 km. This secondary peak, seen only in the eyewall region, is likely caused by an accumulation of graupel and snow at the top of vigorous updrafts in the eyewall. Above this secondary peak, the reflectivity continues its sharp drop, resulting in a value of 18 dBZ in the upper troposphere near 15 km. Values of reflectivity for the rainband and stratiform regions are lower than the eyewall in the observations, with mean reflectivities of around 30 dBZ in the lower troposphere dropping to about 10 dBZ at 15 km.

The simulations show the bias toward high reflectivity discussed previously. Simulated mean eyewall reflectivities are much higher than observed, with low-level values approaching 48 dBZ. There is no peak in mean reflectivity at the melting level, only a quicker decrease with height between 4 and 5 km. Above this level the reflectivity continues to decrease, but not as rapidly as the observed reflectivity. Above 12 km the reflectivity does begin to decrease rapidly, but it remains significantly greater than the observed reflectivity all the way up to 15 km. Differences between the observed and simulated reflectivity are significant at the 99% confidence level at all levels in all three regions. The high reflectivity bias seen in the model values could be at least partially attributable to the way in which reflectivity is calculated in the model (see Section 2). Further discussion of this possibility is provided in Section 4.

The vertical motion data was then separated into updraft and downdraft subsamples (Fig.5). The observed eyewall mean updrafts are slightly stronger than the rainband updrafts (at about 2-2.5 m s^{-1} in the mid- to upper-troposphere), while the observed stratiform updrafts range between 1 and 2 m s^{-1} at the same levels. Downdrafts in the observations are much stronger in the eyewall region than in the rainband region above the melting level. Below the melting level, downdrafts are about the same magnitude. In the observed stratiform regions, mean downdrafts remain at nearly 1 m s^{-1} throughout

the depth of the troposphere. The upward motion in all regions of the observations increases in the upper troposphere. This was hypothesized in Black et al. (1996) to occur as the updrafts lose their hydrometeors and water loading effects are reduced. It could also be partially attributable to the fact that at higher altitudes the radar is capable of measuring fewer points, since there are fewer scatterers at those levels to produce a measurable radar return.

In the simulations, mean updrafts are strongest in the eyewall region and weakest in the stratiform region, similar to the observations. Values of the mean simulated eyewall and stratiform updrafts are about 30-50% less than the mean observed eyewall and stratiform updrafts, respectively, while they are about identical for the rainband updrafts. In contrast to the observations, the mean eyewall downward motion in the simulations is significantly weaker than the mean upward motion, while in the stratiform region the downward and upward motions are of a comparable magnitude. Another significant difference between the simulations and the observations is that in the simulations the upward motion decreases in the upper troposphere for all regions, while in the observations the upward motion increases with increasing height. Differences between the observations and simulations are significant at the 99% confidence level for both updrafts and downdrafts over the entire troposphere for the eyewall and stratiform regions, and over portions of the troposphere for the rainband region.

b) Distributions

While profiles of mean values can yield valuable information regarding the mean structure of a given variable, they do not show the distributions of variables and how those distributions vary with height. Such information can be gleaned by examining contoured frequency by altitude diagrams (CFADs; see section 2c). Figure 6 shows CFADs of vertical motion for the observations and simulations sorted into eyewall, rainband, and stratiform regions. As in Black et al. (1996), the majority of vertical motions are weak ($|w| < 2$ m s^{-1}), but a small fraction (1-2%) of up- and downdrafts exceed 6 m s^{-1}. The observed distributions of vertical motion are the broadest for the eyewall region and the narrowest for the stratiform region. Values of observed vertical motion in the eyewall range from –6 to 9 m s^{-1} below the melting level. The distributions are fairly constant with height below the

melting level, but they broaden with height above, indicating strong up- and downdrafts aloft for the extreme events (from –12 m s^{-1} to 12 m s^{-1}) at 13 km. The maximum frequency (*i.e.,* mode) of observed vertical motions is slightly negative in the lowest 2 km, but it becomes near zero or slightly positive above there. Above 9 km the mode of vertical motion is clearly upward, reflecting the loss of hydrometeors and reduction in water loading in the upper levels, similar to what was seen in the observed mean eyewall updraft profile in Fig. 5a. The observed rainband and stratiform CFADs (Figs. 6c and e) are narrower than the observed eyewall CFAD. They both also show a pronounced narrowing above the melting level, and the modal rainband vertical motion below the melting level is about –1.5 m s^{-1}, suggesting that at least some of the rainband sample in the observational database contains strong stratiform precipitation. Modal vertical motions in both regions become positive above 10-11 km. The sharp kink in the rainband vertical motion distribution at the melting level (4 km) is likely at least partially attributable to fall speed estimation errors that are magnified by the relatively smaller number of data points in the rainband region (cf. Table 2). Unlike the eyewall region, the distribution of observed vertical motion above the melting level is nearly constant with height in the rainband regions.

In contrast to the observations, the simulated vertical motion CFADs show a narrower distribution of vertical velocities. The majority of simulated up- and downdrafts are weak, similar to the observations, but values of the maxima are less than the observed values. In the eyewall (Fig. 6b), values in the lower troposphere range from –3 to 4 m s^{-1}. The range of upward motions increases with increasing height up to the melting level at 5-6 km, at which point the top 1% of points have upward motion of about 8 m s^{-1}. Above the melting level the maximum values decrease, but then there is another relative maximum at about 10 km. Above 10 km, the distribution narrows, in contrast to the observed distributions. The modal values in the eyewall are about zero in the lowest 2 km and become negative up until 8 km, above which it becomes slightly positive. As in the observations, the rainband distribution is narrower than the eyewall, and the stratiform distribution is narrower than the rainband. The simulated rainband distribution shows a similar pattern to the eyewall, with increasing maximum upward motions up to the melting level, followed by a drop off and a secondary maximum at 10 km,

and decreasing upward motion above that. An inspection of CFADs of simulated snow and graupel mixing ratios in the rainband region (Fig. 7) indicates that this secondary maximum of upward motion at 10 km is associated with a sharp decrease in graupel and a maximum in snow, suggesting that the secondary peak is related to a decrease in water loading as the graupel particles fall from the updrafts between 7 and 9 km. The stratiform distribution of vertical velocity (Fig. 6f) is very compact, with values ranging between about –3 and 3 m s^{-1} for nearly the entire depth of the troposphere. The distribution of vertical motion is nearly constant with height in the stratiform region. In both the stratiform and rainband regions the modal vertical motion is slightly negative from the surface to 12-13 km, where it becomes zero. In all three regions the downdrafts never exceed 5 m s^{-1}.

The observed reflectivity CFADs (Fig. 8) show differences across the three regions. The eyewall CFAD is the most broadly distributed, with peak values around 45 dBZ in the lowest 2 km and values as high as 30 dBZ at 12 km for the top 1% of points. In all three regions, the distribution shows a slight decrease in reflectivity with height in the lowest 1-2 km, and then the values increase with height up to the melting level as warm rain processes cause an increase in hydrometeor mixing ratios. Also in all three regions, the distributions show a maximum in reflectivity at the melting level, followed by a sharp drop-off above the melting level. The rate of decrease is higher for the stratiform region than for the eyewall because the eyewall contains stronger updrafts that can transport hydrometeors to higher levels before they fall out (Black et al. 1996). The modal values of reflectivity are different for the three regions as well, with values of 30 dBZ in the lower troposphere in the eyewall region, 25 dBZ in the rainband region, and 20-25 dBZ in the stratiform region.

In the simulations (Figs. 8b,d, and f), the eyewall CFAD shows the broadest distribution of reflectivity, similar to the observations. The high reflectivity bias commonly seen in simulations is clear in these figures, as values approach 60 dBZ for the top 1% of points and the mode in the lowest 3 km is around 40-45 dBZ for the eyewall, 40 dBZ for the rainband, and 25-30 dBZ for the stratiform region. At 6.5 km in the eyewall, the 45 dBZ value comprises nearly 15% of the points in the simulations, but it comprises only 0.7% of the points in the observations. The values of reflectivity in the top 20% of the distribution remain nearly constant or decrease slightly with height below the

melting level. This slope is seen in the other two regions as well, and it is in contrast to the observations, which show an increase in height between about 2 km and the melting level. Also for all three regions in the simulations, there is no maximum in reflectivity at the melting level. This is likely just due to the fact that the model does not account for frozen aggregates with liquid water coating the surface, which is the cause of most bright bands in radar observations. A significant difference between the CFADs of observed and simulated reflectivity is the fact that the decrease with height of reflectivity above 5 km is much smaller in the simulations than in the observations. The ramifications of this difference are discussed later.

A comparison of the distributions of hydrometeors taken from PMS probe measurements and flight-level vertical motions from flights into Hurricane Bonnie on the NASA DC-8 on 26 August 1998 with the simulation of Hurricane Bonnie (Fig. 9) show other notable differences between the observations and the simulation. The portions of the flight patterns selected for the comparisons were when the DC-8 was flying well above the melting level (about 10 km, or temperature ranges between –20 and –25 ˚C). The flight consisted of passes through both cloudy and clear air. The vertical motion PDF (Fig. 9a) is generally similar for both the model and the flight-level data. Similar to the CFADs of vertical motion (cf. Fig. 6), the majority of the values of vertical motion are near zero in both the flight-level data and the simulation. There are more occurrences of stronger simulated vertical motions for this sample, however. Peak values of vertical motion for the flight-level data range between –1.2 and 1.5 m s^{-1}, while in the simulation there is a small number of points (~1%) with vertical motions greater than 1.5 m s^{-1}.

While the PDFs of vertical motion are generally similar for the observations and the simulation, there are more significant differences in the distribution of ice mixing ratios (Fig. 9b). The distribution of ice particles at 9.9 km from the 2D-C probe on the DC-8 shows the majority of values (75%) are less than 0.1 g kg^{-1}. About 7.5% of all values are $\geq$ 0.2 g kg^{-1}, but there are no values greater than 0.4 g kg^{-1}. In the simulation of Bonnie, there is a smaller percentage of values that are less than 0.1 g kg^{-1}, but nearly 23% of the values are $\geq$ 0.2 g kg^{-1}. In addition, some outliers are as large as 0.55 g kg^{-1}.

This discrepancy is consistent with the high bias seen in the simulated reflectivity fields in this and other studies.

c) Correlations

A scatter plot of flight-level vertical motion and probe measurements of hydrometeor mixing ratio for a portion of the flight track used in Fig. 9 is compared with a scatter plot from an equivalent "flight-level" measurement from the model (Fig 10). The subsample of the flight track used in the observations was taken through a line of mixed convective and stratiform rain. An equivalent measurement from the model was taken through a similar feature at a similar time in the simulation. As indicated by the linear regression lines fit to each distribution, there is virtually no relationship between observed vertical motion and mixing ratio at 9.9 km. The percent of variance explained by the regression line (r^2) is less than 1%. In the model, however, there is a much stronger relationship. Values of cloud ice mixing ratio are less than 0.4 g kg^{-1} for updrafts weaker than 0.5 m s^{-1}, and they show a steadily increasing value for increasing updraft strengths. The value of r^2 for this regression is about 58%. A Student's t-test calculation was performed to determine the level of statistical signficance at which the correlation coefficient (r) can be considered to be nonzero. The correlation coefficient in the observed distribution is nonzero only at the α=0.5 significance level, compared with the distribution in the simulation, which is nonzero at the α=0.002 level, indicating a much higher confidence in the strength of the relationship in the simulation.

A comparison similar to that done in Fig. 10 was performed for vertical motion and reflectivity from the radar dataset and the simulations of both Bonnie and Floyd (Fig. 11). Comparing an independent dataset with the simulations will test the robustness of the relationships shown in Fig. 10. Furthermore, the sampling volume for the flight-level vertical motion and the probe measurements is quite small, so definitive conclusions on the relationships between vertical motion and hydrometeor mixing ratio based solely on these fields are dubious. From the radar data (Fig. 11a), there is a fair amount of scatter between observed reflectivity and vertical motion at 9.9 km. Two separate linear regression lines were calculated in each of the figures shown in Fig. 11: one for vertical motions greater than 1.5 m s^{-1} and one for vertical motions less than -1.5 m s^{-1}. The slopes (% variance

explained) of the regression line for the updrafts is 0.784 (9%) and for the downdrafts it is –0.5354 (2%), respectively. By contrast, the slopes (% variance explained) of the regression lines for the updrafts and downdrafts for the simulations are 1.6255 (22%) and –3.033 (2%), respectively, indicative of a stronger relationship between vertical motion and reflectivity in the simulations.

A similar scatter plot was constructed at 3.6 km, which was below the melting level with temperatures ranging between 6 and 10 ˚C. The same contrast between the observations and the simulations is evident at 3.6 km (Fig. 11c,d), where the slopes of the regression lines for the updrafts (downdrafts) for the observations are 0.1806 (-0.5366) and for the simulations they are 1.68 (-7.1604). The amount of variance explained in the updrafts (downdrafts) in the observations is 0.1% (0.4%) and in the simulations it is 18% (10%). In addition to the stronger relationship between reflectivity and vertical motion seen in the simulations from these scatter plots, the high bias in simulated reflectivity relative to the observations is seen by comparing the y-intercepts of the regression equations. For the observations, the y-intercept for the updraft regression equation at 9.9 km is about 14 dBZ, while for the simulations it is about 27 dBZ. At 3.6 km, the y-intercept for the observations is 32 dBZ, while for the simulations it is 42 dBZ. Student's t-test comparisons of the correlation coefficients for these distributions, similar to what was calculated for the microphysical probe measurements (cf. Fig. 10), were calculated for the distributions in Fig. 11. For the observations, the only distribution that had a nonzero value of r significant at less than the 0.05 level was the observed updraft distribution at 9.9 km (the other distributions were significant at the 0.2 level or greater). In contrast, the simulation has nonzero values of r significant at less than or equal to the 0.005 level for updrafts at 9.9 km and both updrafts and downdrafts at 3.6 km.

Figure 12 shows comparisons of the mean reflectivity within a vertical velocity bin as a function of height. Similar to the scatter plots in Fig. 11, there is a suggestion of a weak relationship between observed reflectivity and vertical motion. Between 3 and 5 km altitude, observed reflectivity values increase slowly as upward motion increases from 0 to 9 m s^{-1} (e.g., increasing from 37 dBZ for the 0 m s^{-1} bin to 47 dBZ for the 6 m s^{-1} bin at the 4-km level). Above the melting level, between 7 and 12 km altitude, there is again a weak relationship between vertical motion and reflectivity, for both

up- and downdrafts. As in the flight-level data, the relationship between vertical motion and reflectivity is much stronger for the simulations. The slope of the relationship is very pronounced for the weak vertical motions (i.e., between –2 and 2 m s^{-1}), but there is a noticeable slope even for the vertical motion values exceeding 9 m s^{-1}. The differences in the strength of the relationship between the observed and simulated reflectivity shown in Figs. 11 and 12 are consistent with the differences in the probe data.

4. Discussion

a) Summary of comparisons

The comparisons presented here show that the model reproduces many of the gross features seen in the observations. For example, profiles of both observations and simulations show increasing vertical motion and decreasing reflectivity with height above the melting level, the upward motion is strongest and the distributions of vertical motion and reflectivity are broadest in the eyewall and weakest and narrowest in the stratiform regions, and the majority of the vertical motion is weak in all regions. Despite these similarities, there are many significant differences between the observations and the simulations that suggest notable biases in the simulations:

- Magnitudes of simulated mean vertical motion are lower than the observations, and magnitudes of simulated mean reflectivity are higher than the observations throughout the troposphere;
- Mean updrafts and downdrafts are weaker in simulations than in the observations;
- Reflectivity decreases much more slowly with height above the 0˚C level in the simulations than it does in the observations;
- There is no increase in reflectivity with height below the 0˚C level in the simulations;
- Distributions of vertical motion and reflectivity are narrower for the simulations than for the observations;
- Modal and maximum vertical motions are lower in simulations, reflectivities are higher in simulations;

- Distribution of simulated vertical motion narrows with height in the upper troposphere, in contrast to the observed vertical motion, which broadens with height;
- Slope of decrease of reflectivity above the melting level for top 10% of distribution of points in simulation much smaller than in observations;
- Correlation between vertical motion and hydrometeor mixing ratio/reflectivity is much stronger in simulations than in the observations;

b) Relevance to microphysical scheme

Before considering the possibility that differences between the observations and simulations are attributable to deficiencies in the microphysical scheme, it is first necessary to consider other sources of differences between the datasets. For example, the vertical motions in the model are consistently weaker than the observations. This could be partially due to the fact that the resolution of the model is coarser than the effective resolution of the radar data (1.67 km grid length for the model vs. 1.5 km for the VI radar beam). While this may explain some of the differences in the magnitudes of the vertical motion values, it is not a sufficient explanation for the vertical variation in the vertical motion field, nor does it explain differences in the relationships between the vertical motions and hydrometeor mixing ratios and reflectivities.

Another marked difference is between the magnitude of the radar reflectivities calculated from the model and those measured by the radar. As discussed in Section 2, the reflectivity in the model is calculated using the total mass content of each individual constituent (precipitating) species and adding their reflectivity values together to yield a total reflectivity value. The relationship expressed in Section 2 (see Eq. 4) is essentially a Z-M relationship of the form

$$Z = aM^b. \tag{6}$$

For the model calculations used here, the value of b is 1.75, while the value of the a parameter ranges from 1228 for snow to 20417 for rain. When there is a mixture of particle types at a grid point, the effective Z-M relation is a mixture of the constituent Z-M curves. Figure 13 shows the Z-M relations used for each constituent species in the model compared with Z-M relations determined empirically from probe measurements in various hurricanes (Willis and Jorgensen 1982, Black 1990). In Fig. 13a

there is also a curve obtained by plotting calculated Z vs. M for regions in the Bonnie simulation between –3 and –8 ˚C for three different times during the simulation. At the altitudes in Fig. 13a there is a mixture of snow and graupel, and the fitted Z-M relation varies between each of these species. Thus the effective Z-M relation used in these calculations can be significantly different from the prescribed value when there is a mixture of species. The observed Z-M relations shown in Fig. 13a were determined from measurements taken between –3 and –8 ˚C in two storms, Hurricanes Norbert and Irene (Black 1990). The Z-M relations used in the model are significantly different from those determined from Black (1990), especially when compared against a more stratiform storm, Norbert (Black 1990). Values of reflectivity in the relationship used in the model are consistently higher for higher values of water content. Figure 13b shows a comparison between the model Z-M relation for rain and measurements collected in three hurricanes, Anita (1977), Frederic (1979), and David (1979). From this comparison differences are again seen between the relation used in the model and that determined from observations, with higher values of reflectivity seen in the model for the higher water contents.

To test the significance of using a different model Z-M relation in explaining the bias in the model-derived reflectivity, model reflectivities are recalculated using the empirically-derived relations (see Fig. 13) from Willis and Jorgensen (1982) for levels below the melting level and Black (1990) for levels above the melting level. Figure 14 shows reflectivity profiles for all points from the Floyd and Bonnie simulations using these alternate Z-M relations, as well as the reflectivity for all points in the VI database. Using different relations does produce significant differences in the reflectivity profiles above the melting level. Using different ice relations, the reflectivity is reduced by nearly 10 dBZ above the melting level when using a relation characteristic of a convective storm and 15 dBZ when using a relation taken from a stratiform storm. In both of these modified profiles, however, the reflectivity decrease with height above 7.5 km is still less than the observed decrease with height. Using the different rain relation does reduce the reflectivity about 2-3 dBZ, but this value is still much higher than the observed reflectivity. It must also be emphasized that using a different Z-M relation implicitly means using different assumptions regarding intercept parameter and particle density (cf. Eq.

5). In order to gain a true understanding of the impact of varying these parameters, they must also be changed in the scheme itself and the simulation must be re-run using these new values.

Despite the sources of biases in the simulation discussed above (i.e., resolution differences, Z-M relation differences), many of the differences between the observations and the simulations are likely attributable to biases in the microphysical parameterization scheme. One of the most apparent biases suggested by these results is that water loading is too prominent a factor in the simulations. This is supported by several differences between the simulations and the observations: the simulations consistently underdevelop the strongest vertical velocities and overdevelop the highest reflectivities, in all regions; the correlation between vertical motion and reflectivity and vertical motion and hydrometeor concentration is much stronger in the simulations than in the observations; the reflectivity decreases much more slowly with height above the melting level in the simulations than in the observations; the downdraft profiles in the simulations are not reproduced well (e.g., in the differences between convective vs. non-convective storms), and the distribution of simulated vertical motion narrows with height in the upper troposphere, in contrast to the observed vertical motion, which broadens with height. The likely culprit for the water loading problem is an underestimate of hydrometeor fall speed. When fall speeds are underestimated, hydrometeors reside in a model layer longer than they should, resulting in increased water loading, reduced updrafts, enhanced reflectivity, and a decrease of reflectivity with height that is too slow for a given updraft magnitude.

Another bias evident from the comparisons is that the there is too much hydrometeor mass . This bias likely stems from the fact that either the production terms of rain and frozen precipitating particles are too strong or the conversion terms are too weak (or some combination of both). This possibility is evidenced by the fact that the vertical velocities are too weak in the simulations and the reflectivity decreases too slowly with height above the melting level. The production of the frozen precipitating particles, graupel and snow, may be the source of the problem here. The overproduction of these species, combined with lower fall speeds for snow, leads to weaker updrafts through water loading and reflectivities that are too high and that extend over too great a vertical distance.

Furthermore, the melting of graupel (and to some extent snow) as it falls would cause higher rain mass contents and reflectivities below the melting level when graupel is overproduced.

Many of the biases summarized above may arise from the fact that many of the relationships and assumptions underlying microphysical parameterization schemes were derived from clouds that were not associated with tropical cyclones. For example, the drop size distributions for the various species should be investigated to determine if they need to be modified to be appropriate for tropical cyclone environments. This is not a straightforward task, however, since size distributions are highly variable from case to case, and they can even vary across different locations within the same storm. To illustrate this point, Figure 15 shows size distributions from PMS monoprobe data from a single flight into Hurricane Emily of 1987 (Black et al. 1995). The size distributions shown here were taken by averaging the distributions during the times that the aircraft was in either the eyewall or the stratiform regions of the storm. For this calculation "eyewall" was defined as when the aircraft was within three minutes of the center of the storm and the magnitude of the flight-level vertical motion was > 2 m s^{-1}, while "stratiform" was defined as all times when the aircraft was at least two minutes outside of the eyewall and the flight-level vertical motion was less than 2 m s^{-1}. As can be seen by Fig. 15, there are notable differences in the size distributions in the eyewall compared with the stratiform areas of the storm. There are more particles in the eyewall region of the storm, a difference reflected in the different intercept parameters (N_0) of the two size distributions (differences significant at the 99.5% confidence level). Such spatial variability illustrates the complexity of applying bulk parameterization schemes to tropical cyclone environments and other environments with similar variability.

Many aspects of the production and conversion terms in the parameterization scheme have also been identified as possible deficiencies. For example, the autoconversion of cloud water to rain water and cloud ice to snow and graupel is one area that could be modified to produce schemes that are capable of responding to differing air masses (e.g., Tripoli and Cotton 1980). Another possible modification is to have separate classes for graupel and hail (Ferrier 1994, Ferrier et al. 1995), and to make the generation of graupel dependent on updraft magnitude and liquid water content. The parameterization of vapor deposition should include new measurements of saturation vapor pressure

with respect to supercooled water (Fukuta and Gramada 2000), the freezing of rain to form graupel should be made to be dependent on the ice nucleation process, and the high temperature dependence of the aggregation of cloud ice should be investigated.

The changes discussed above will be tested in the model, and their impact on the vertical motion, hydrometeor mixing ratio, and reflectivity statistics from the simulations will be tested against the observations using the techniques presented here. These results will be the subject of an upcoming paper.

5. Concluding remarks

The biases indicated by the comparisons between simulations and observations shown here can have important implications for the ability of high-resolution simulations to better predict tropical cyclone intensity and rainfall. Accurate distributions of hydrometeors and their linkages with the vertical velocity field are crucial for obtaining accurate distributions of condensation, evaporation, freezing, melting, deposition, and sublimation in time and space. Since latent heating is the major source of energy for a tropical cyclone, improvements in prescribing their distributions will lead to improvements in tropical cyclone intensity and rainfall prediction. In addition to improving intensity and rainfall predictions, improving the distribution of latent heating can lead to better forecasts of storm structure. Many simulations of tropical cyclones have storms whose wind and rain fields are too broad. Some of this is likely due to resolution limitations, but some is also probably because the strength of the secondary circulation is too weak. By increasing the mean vertical motion in the eyewall, the strength of the cyclone's secondary circulation will be enhanced. The stronger radial inflow may lead to smaller, more compact storms and more accurate wind and rain fields in the simulations. Of course it could also lead to more intense storms, which may or may not be a desirable result. Such relationships are quite complex, and they require further investigation.

Many of the biases revealed by these comparisons arise because the microphysical parameterization scheme is a bin microphysics scheme. Such a scheme requires certain assumptions, such as those regarding size distributions and fall speeds, that may play a significant role in

determining the relationship between vertical motion and hydrometeor mixing ratio. More sophisticated schemes that predict more variables explicitly, such as double-moment schemes and spectral schemes, may alleviate some of the uncertainties mentioned here, but they have other assumptions in their formulations and they are much more costly and time-consuming to run.

The value of the comparison techniques shown here is twofold. First, because the comparisons are statistical in nature, they do not require a precise matching of features between the observations and the simulations. This is advantageous, since it is beyond the realm of predictability to be able to exactly reproduce the timing and location of vertical motion maxima/minima and convective and stratiform features. Second, this technique is adaptable to a variety of model configurations and observational platforms. Future work will involve implementing improvements to the existing microphysical parameterization scheme based on the biases illustrated here and testing these improvements using the framework provided here. Other microphysical schemes, such as double-moment and spectral schemes, can be tested as well. In this sense these evaluation techniques can be used to compare not only parameterization schemes to observations, but also different parameterization schemes to each other. Additional observational platforms, such as TRMM PR reflectivity fields and NASA EDOP vertical velocity and reflectivity fields from the NASA ER-2 aircraft, can also be compared with the high-resolution simulations.

Current operational models, such as the GFS and the Geophysical Fluid Dynamics Laboratory model, do not explicitly account for hydrometeors in their model. Rather, they use a simple removal of supersaturation and they parameterize the evaporation of falling rain. The techniques used to evaluate the scheme shown here nevertheless can easily be used to evaluate the schemes in these operational models to highlight areas in need of improvement. While adding complexity to the operational schemes may be impractical due to computational efficiency limitations and operational constraints (and may actually add little to improve the forecasts), advances in computing power will enable more complex schemes to be implemented in the future, if needed. Furthermore, as the Weather Research and Forecast (WRF) model becomes operational in the next couple of years, the possibility of

implementing more sophisticated physical parameterizations will increase. Such improvements hold the potential of improving our forecasting of tropical cyclone intensity and rainfall.

Acknowledgements

Our thanks go to many people who helped in the preparation of this manuscript. Frank Marks and Paul Willis of HRD provided many helpful comments and suggestions to improve the work, as did Chris Landsea and Shirley Murillo, also of HRD. Scott Braun of NASA/GSFC also provided helpful suggestions and stimulating discussions about the use of microphysical parameterization schemes in hurricane environments. Our thanks also go to Tim Marchok of NOAA/GFDL, who provided information about microphysical parameterizations used in the operational models, and to Nancy Griffin of HRD who provided radar images to us. Finally, Joe Tenerelli of RSMAS/University of Miami was very helpful in providing assistance with the simulations.

This work was partially supported by NOAA base funds and by a grant from NASA, Grant number S-44774-X, as a part of the CAMEX-IV field program. Computing resources were provided by funding from the Office of Naval Research. This research was carried out (in part) under the auspices of the Cooperative Institute for Marine and Atmospheric Studies (CIMAS), a joint institute of the University of Miami and NOAA, cooperative agreement #NA67RJ0149.

References

Black, M.L., R.W. Burpee, and F.D. Marks, Jr., 1996: Vertical motion characteristics of tropical cyclones determined with airborne Doppler radial velocities. *J. Atmos. Sci.*, **53**, 1887-1909.

Black, R.A., 1990: Radar reflectivity-ice water content relationships for use above the melting level in hurricanes. *J. Appl. Meteor.*, **29**, 955-961.

Black, R.A., and J. Hallett, 1986: Observations of the distribution of ice in hurricanes. *J. Atmos. Sci.*, **43**, 802-822.

Braun, S.A., and R.A. Houze, 1994: The transition zone and secondary maximum of radar reflectivity behind a midlatitude squall line: Results retrieved from Doppler radar data. *J. Atmos. Sci.*, **51**, 2733-2755.

Braun, S.A. and W.-K. Tao, 2000: Sensitivity of high-resolution simulations of Hurricane Bob (1991) to planetary boundary layer parameterizations. *Mon. Wea. Rev.*, **128**, 3941-3961.

Braun, S.A., 2002: A cloud-resolving simulation of Hurricane Bob (1991): Storm structure and eyewall buoyancy. *Mon. Wea. Rev.,* **130**, 1573-1592.

Cotton, W.R., M.S. Stephens, T. Nehrkorn, and G.J. Tripoli, 1982: The Colorado State University three-dimensional cloud-mesoscale model –1982. Part II: An ice-phase parameterization. *J. Rech. Atmos*., **16**, 295-320.

Dudhia, J., 1989: Numerical study of convection observed during the Winter Monsoon Experiment using a mesoscale two-dimensional model. *J. Atmos. Sci.*, **46**, 3077-3107.

Farley, R.D., and H.D. Orville, 1986: Numerical modeling of hailstorms and hailstone growth. Part I: Preliminary mdoel verification and sensitivity tests. *J. Climate Appl. Meteor*., **25**, 2014-2035.

Ferrier, B.S., 1994: A double-moment multiple-phase four-class bulk ice scheme. Part I: Description. *J. Atmos. Sci*., **51**, 249-280.

Ferrier, B.S., W.-K. Tao, and J. Simpson, 1995: A double-moment multiple-phase four-class bulk ice scheme. Part II: Simulations of convective storms in different large-scale environments and comparisons with other bulk parameterizations. *J. Atmos. Sci*., **52**, 1001-1033.

Fovell, R.G., and Y. Ogura, 1988: Numerical simulation of a midlatitude squall line in two dimensions. *J. Atmos. Sci.*, **45**, 3846-3879.

Fukuta, N. and C.M. Gramada, 2003: Vapor pressure measurement of supercooled water. *J. Atmos. Sci.*, **60**, 1871-1875.

Grell, G.A., J. Dudhia, and D.R. Stauffer, 1994: A description of the fifth generation Penn State/NCAR Mesoscale Model (MM5). NCAR Tech. Note NCAR/TN-398 + STR, 138 pp.

Hall, W.D., 1980: A detailed microphysical model within a two-dimensional dynamic framework: Model description and preliminary results. *J. Atmos. Sci*., **37**, 2486-2507.

Hsie, E.-Y., Anthes, R.A., and D. Keyser, 1984: Numerical simulation of frontogenesis in a moist atmosphere. J. *Atmos. Sci*., **41**, 2581-2594.

Jorgensen, D.P., and M.A. LeMone, 1989: Vertical velocity characteristics of oceanic convection. *J. Atmos. Sci.,* **46**, 621-640.

Jorgensen, D.P., T.J. Matejka, D. Johnson, and M.A. LeMone, 1994: A TOGA-COARE squall line seen by multiple airborne Doppler radars. Preprints, *Sixth Conf. On Mesoscale Processes*, Portland, OR, Amer. Meteor. Soc., 25-28.

Kain, J.S., and J.M. Fritsch, 1993: Convective parameterization for mesoscale models: The Kain-Fritsch scheme. *The Representation of Cumulus Convection in Numerical Models, Meteorl. Monogr.,* No. 46, Amer. Meteor. Soc., 165-170.

Karyampudi, V. M., G.S. Lai, and J. Manobianco, 1998: Impact of Initial Conditions, Rainfall Assimilation, and Cumulus Parameterization on Simulations of Hurricane Florence (1988). *Mon. Wea. Rev.*, **126**, 3077–3101.

Lawrence, M.B., L.A. Avila, J.L. Beven, J.L. Franklin, J.L. Guiney, and R.J. Pasch, 2001: Atlantic Hurricane Season of 1999. *Mon. Wea. Rev*. **129**, 3057–3084.

Lin, Y.-L., R.D. Farley, and H.D. Orville, 1983: Bulk parameterization of the snow field in a cloud model. *J. Climate Appl. Meteor.*, **22**, 1065-1092.

Liu, Y., D.-L. Zhang, and M.K. Yau, 1997: A multiscale numerical study of Hurricane Andrew (1992). Part I: Explicit simulation and verification. *Mon. Wea. Rev*., **125**, 3073-3093.

Lord, S.J., H.E. Willoughby, and J.M. Piotrowicz, 1984: Role of a parameterized ice-phase microphysics in an axisymmetric nonhydrostatic tropical cyclone model. *J. Atmos. Sci.*, **41**, 2836-2848.

McCumber, M., W.-K. Tao, J. Simpson, R. Penc, and S.-T. Soong, 1991: Comparison of ice-phase microphysical parameterization schemes using numerical simulation of tropical convection. *J. Appl. Meteor*., **30**, 985-1004.

Marks, F.D., and R.A. Houze, Jr., 1987: Inner core structure of Hurricane Alicia from airborne Doppler radar observations. *J. Atmos. Sci.,* **44**, 1296-1317.

Marshall, J.S., and W. McK. Palmer, 1948: The distribution of raindrops with size. *J. Meteor.,* **5**, 165-166.

Orndorff, C., S.S. Chen, and J.E. Tenerelli, 2002: Precipitation and landmass interaction during Hurricane Georges (1998) landfall at Puerto Rico. Preprints, Twenty-fifth Conference on Hurricanes and Tropical Meteorology, 29 April – 3 May 2002, San Diego, CA, 297-298.

Pagowski, M., and G.W.K. Moore, 2001: A numerical study of an extreme cold-air outbreak over the Labrador Sea: Sea ice, air-sea interaction, and development of polar lows. *Mon. Wea. Rev.*, **129**, 47-72.

Pasch, R.J., L.A. Avila, and J.L. Guiney, 2001: Atlantic Hurricane Season of 1998. *Mon. Wea. Rev.*, **129**, 3085-3123.

Rappaport, E.N., 2000: Loss of life in the United States associated with recent Atlantic tropical cyclones. *Bull. of Amer. Met. Soc.*, **81**, 2065–2074.

Rogers, R.F., S.S. Chen, J.E. Tenerelli, and H.E. Willoughby, 2003: A numerical study of the impact of vertical shear on the distribution of rainfall in Hurricane Bonnie (1998). *Mon. Wea. Rev.*, **131**, 1577-1599.

Rutledge, S.A., and P.V. Hobbs, 1984: The mesoscale and microscale structure and organization of clouds and precipitation in midlatitude cyclones. Part XII: A diagnostic modeling study of precipitation development in narrow cold-frontal rainbands. *J. Atmos. Sci*., **41**, 2949-2972.

Tao, W.-K., and J. Simpson, 1993: The Goddard cumulus ensemble model. Part I: Model description. *Terr. Atmos. Oceanic Sci*., **4**, 35-72.

Tenerelli, J.E., and S.S. Chen, 2002: Intensity change and eyewall replacement in Hurricane Floyd (1999). Preprints, Twenty-fifth Conference on Hurricanes and Tropical Meteorology, 29 April – 3 May 2002, San Diego, CA, 168-169.

Tripoli, G.J., and W.R. Cotton, 1980: A numerical investigation of several factors contributing to the observed variable intensity of deep convection over South Florida. *J. Appl. Meteor.*, **19**, 1037-1063.

Willoughby, H.E., F.D. Marks, and R.J. Feinberg, 1984: Stationary and moving convective bands in hurricanes. *J. Atmos. Sci.*, **41**, 3189-3211.

Willoughby, H.E., 1995: Mature structure and evolution, from "Global Perspectives on Tropical Cyclones," Ed. R.E. Elsberry, WMO/TD-No. 693.

Yuter, S.E., and R.A. Houze, Jr., 1994: Three-dimensional kinematic and microphysical evolution of Florida cumulonimbus. Part III: Vertical mass transport, mass divergence, and synthesis. *Mon. Wea. Rev.,* **123**, 1964-1983.

Zhang, D.-L., and R.A. Anthes, 1982: A high-resolution model of the planetary boundary layer – sensitivity tests and comparisons with SESAME-79 data. *J. Appl. Meteor.*, **21**, 1594-1609.

Zhang, D.-L., 1989: The effect of parameterized ice microphysics on the simulation of vortex circulation with a mesoscale hydrostatic model. *Tellus*, 41A, 132-147.

Zhang, D.-L., Y. Liu, and M.K. Yau, 2000: A multiscale numerical study of Hurricane Andrew (1992). Part III: Dynamically-induced vertical motion. *Mon. Wea. Rev*., **128**, 3772-3788.

Zhu, T., D.-L. Zhang, and F. Weng, 2000: Numerical simulation of Hurricane Bonnie (1998) using the advanced microwave sounding unit derived winds. Preprints, Twenty- fourth Conference on Hurricanes and Tropical Meteorology, 29 May – 2 June 2000, Ft. Lauderdale, FL, 460-461.

Appendix A: Classification algorithm for Eyewall, Rainband, and Stratiform regions

Reflectivity is first averaged in two layers, the 0.5–4 km layer (lower-level reflectivity) and the 6-10 km layer (upper-level reflectivity). The eyewall candidate region is identified first. Starting from the center of the grid (i.e., the center of the simulated or observed storm), the upper-level reflectivity is evaluated until the first instance where it exceeds 30 dBZ. From this point, the upper-level reflectivity is evaluated for an additional 15 km. The maximum upper-level reflectivity within this radial band is flagged (r_{upmax}). The lower-level reflectivity is then evaluated in a 20-km radial band centered on the flagged point, and the maximum low-level reflectivity is saved and the radius corresponding to that value is flagged (r_{lowmax}). Moving radially outward from r_{upmax}, the upper-level reflectivity is evaluated until it falls below 70% of the value at r_{upmax}. Additionally, the lower-level reflectivity is evaluated until it falls below 70% of the value at r_{lowmax}. The maximum of these two radii is defined as the outer edge of the eyewall candidate region. Moving radially inward from r_{lowmax}, the lower-level reflectivity is evaluated until it falls below 15 dBZ. This radius is defined as the inner edge of the eyewall candidate region.

Moving radially outward from the eyewall, the rainband candidate regions are next identified. This technique uses nearly the same algorithm as the eyewall determination, with a few minor differences: 1) the initial reflectivity used to flag a possible rainband is 25 dBZ instead of 30 dBZ; 2) only one test is performed to identify the outer edge of the rainband; 3) because of weaker radial gradients in reflectivity at larger radii, the threshold value to identify the outer edge of a rainband is 75% instead of 70% of the maximum upper-level reflectivity; and 4) the criterion for defining the inner edge of a rainband is when the low-level reflectivity falls below 75% of the maximum lower-level reflectivity (rather than a 15 dBZ threshold for the eyewall inner edge).

To identify a stratiform region, all locations that are neither eyewall nor rainband, but where the lower-level reflectivity exceeds 15 dBZ, are considered stratiform regions. All other regions are considered "other", unless the lower-level reflectivity is below 2 dBZ, in which case it is considered to be missing. Because of the high bias of simulated reflectivities when compared to observations (cf.,

for example, Fig. 1), the thresholds used to define a potential eyewall and rainband (30 dBZ and 25 dBZ, respectively) are reduced by 5 dBZ for the observed data. Figure A1 provides a schematic of the definition of the candidate regions.

With the candidate regions identified from the reflectivity fields (Fig. A1), the vertical motion fields are next used to identify the actual eyewall, rainband, and stratiform regions. To preserve radial contiguity, values of the absolute value of vertical motion in the layer between 4 and 10 km are averaged over a 5-km radial distance. If the running mean of vertical motion anywhere within a 5 km distance of the location being considered is greater then 1.5 m s^{-1} within a candidate eyewall (or rainband) region, then that location is identified as part of the eyewall (or rainband). The value of 1.5 m s^{-1} is chosen because that value was found in Black et al. (1996) to define the boundaries of coherent up- and downdrafts in their VI dataset. If no region within 5 km is greater than 1.5 m s^{-1}, that location is considered stratiform.

List of Tables

Table 1. Name of hurricane, date of flight, intensity information during flight, number (n) of radial legs, average length of radial legs, and the maximum and minimum *w* from Doppler data during flight.

Table 2. Characteristics of regions in VI and model data.

List of Figures

Figure 1. Comparison of reflectivities from (a) P-3 lower fuselage radar at 4261 m and (b) MM5 simulation at 600 hPa for Hurricane Floyd on 13 September 1999 (note difference in scales of reflectivity between (a) and (b)).

Figure 2. Plot of observed and simulated (a) track and (b)intensity of Hurricanes Bonnie and Floyd. In both (a) and (b) the solid line is the observed value while the dashed line is the simulated value. Vertical bars in (b) bracket times used in simulations.

Figure 3. Examples of regime identification scheme for radar observations of Hurricane Olivia (1994) and simulation of Hurricane Floyd (1999). Plan view radar images are indicated in (a) and (b), radius-height cross sections are indicated in (c) and (d). Areas identified as eyewall, rainband, and stratiform are identified (note difference in scales of reflectivity between (a) and (b)).

Figure 4. Profiles of Doppler-derived (a, c, and e) and simulated (b, d, and f) mean vertical motion (m s^{-1}) and reflectivity (dBZ) for all storms sorted by region. Vertical shaded bars denote those levels where differences are significant at the 99% confidence level.

Figure 5. Profiles of observed and simulated mean updrafts and downdrafts (m s^{-1}) sorted by region. Vertical shaded bars denote those levels where differences are significant at the 99% confidence level.

Figure 6. Contoured frequency by altitude diagrams (CFADs; shading, %) of Doppler-derived (a, c, and e) and simulated (b, d, and f) vertical motion for all storms sorted by region.

Figure 7. CFADs (shading, %) of simulated (a) snow mixing ratio and (b) graupel mixing ratio for the rainband region in the Bonnie and Floyd simulations.

Figure 8. CFADs (shading, %) of reflectivity for all storms sorted by region.

Figure 9. Probability distribution functions (PDFs; %) of (a) flight-level vertical motion and (b) hydrometeor mixing ratio at 9.9 km for observations and simulation of Bonnie.

Figure 10. Scatter plots of flight-level vertical motion (m s^{-1}) and hydrometeor concentrations (g kg^{-1}) at 9.9 km for (a) observations and (b) simulation of Bonnie

Figure 11. Scatter plots of Doppler-derived vertical motion (m s^{-1}) and reflectivity (dBZ) for all storms.

Figure 12. Mean eyewall reflectivity (shading, dbZ) stratified by Doppler-derived vertical motion bins for all storms.

Figure 13. Comparisons of Z-M relations for (a) ice and (b) rain from simulations and from observed hurricane cases.

Figure 14. Profiles of mean reflectivity (dBZ) for all regions using different Z-M relations.

Figure 15. Average size distributions from 2D-P probe on P-3 aircraft from 22 September 1987 in Hurricane Emily (1987) for (a) eyewall regions and (b) stratiform regions. Altitude of aircraft was 4 km. Values of statistical parameters (mean, standard deviation, sample size) for intercept parameter calculated from each distribution shown in inset.

Figure A1. Schematic showing identification of candidate eyewall, rainband, and stratiform regions based on reflectivity.

Storm	Date yr/mo/da	Minimum Surface Pressure (mb)	Maximum Wind Speed (m s-1)	Radial Legs (n)	Mean Leg Length (km)	Doppler Data Max. *w* (m s-1)	Doppler Data Min. *w* (m s-1)
Elena	85/09/01	952	60	14	64	13	-11
Elena	85/09/02	954	60	14	73	13	-07
Gloria	85/09/24	919	70	04	97	24	-21
Emily+	87/09/22	957	65	18	65	24	-19
Gilbert	88/09/14	892	75	10	96	26	-16
Gabrielle	89/09/03	937	60	12	96	14	-11
Hugo	89/09/17	930	65	12	107	24	-18
Hugo	89/09/18	955	50	06	105	12	-13
Hugo	89/09/19	957	45	03	102	12	-12
Hugo	90/09/21	934	65	10	103	15	-15
Gustav	90/08/27	965	50	06	111	21	-19
Gustav*	90/08/29	960	40	30	92	21	-13
Gustav*	90/08/30	958	50	12	87	11	-08
Gustav	90/08/31	959	50	14	94	10	-05
Jimena	91/09/23	945	60	8	78	18	-16
Olivia*	94/09/24	949	55	28	92	19	-18
Olivia*	94/09/25	924	65	32	93	22	-17

Table 1. Name of hurricane, date of flight, intensity information during flight, number (n) of radial legs, average length of radial legs, and the maximum and minimum *w* from Doppler data during flight.

+ Black et al. (1994) also analyzed these data
* Both NOAA WP-3D aircraft flew concurrently

	Number of occurrences	Percentage of total (%)	Contribution to area (%)
VI data			
Eyewall	836	23.5	15.5
Rainband	137	3.9	4.7
Stratiform	2231	62.7	68.6
Other	352	9.9	11.2
Model data			
Eyewall	49,384	18.6	14.8
Rainband	21,273	8.0	10.7
Stratiform	127,761	48.0	55.1
Other	67,760	25.4	19.4

Table 2. Characteristics of regions in VI and model data.

Observation
2259 UTC 13 September

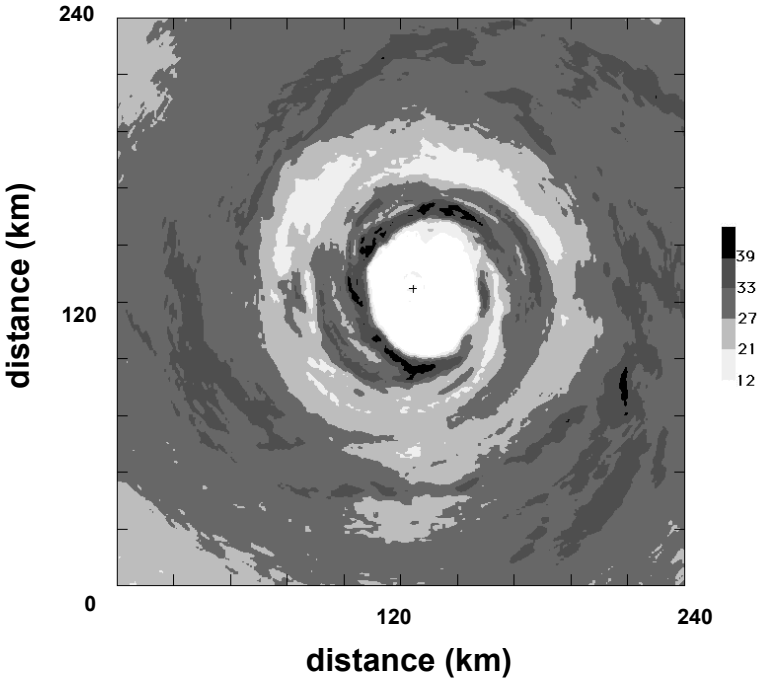

(a)

Simulation
2300 UTC 13 September

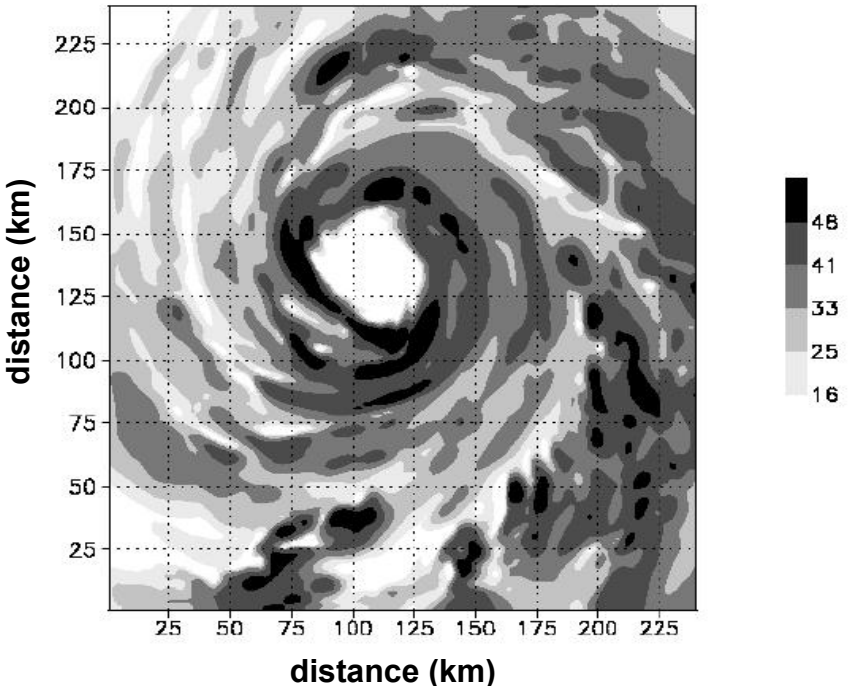

(b)

Figure 1. Comparison of reflectivities from (a) P-3 lower fuselage radar at 4261 m and (b) MM5 simulation at 600 hPa for Hurricane Floyd on 13 September 1999 (note difference in scales of reflectivity between (a) and (b)).

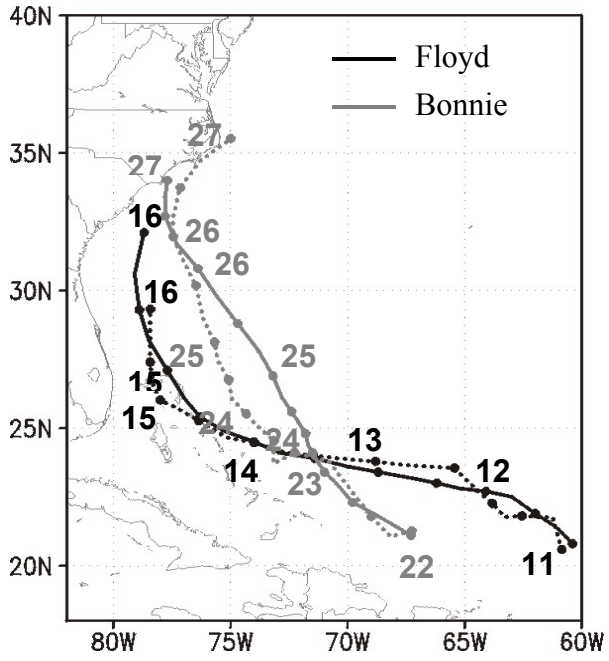

(a)

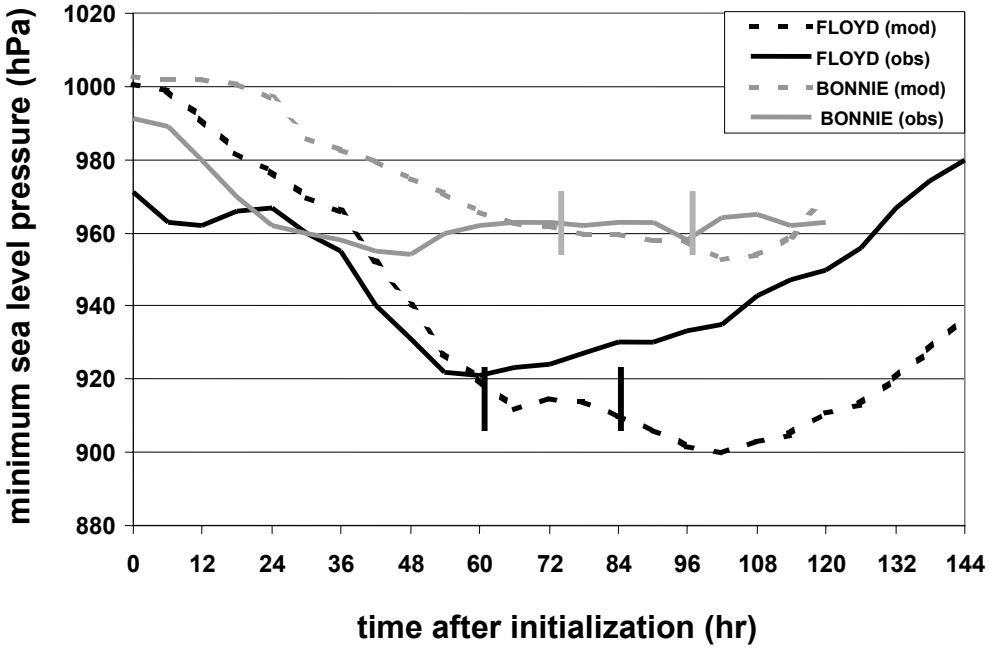

(b)

Figure 2. Plot of observed and simulated (a) track and (b)intensity of Hurricanes Bonnie and Floyd. In both (a) and (b) the solid line is the observed value while the dashed line is the simulated value. Vertical bars in (b) bracket times used in simulations.

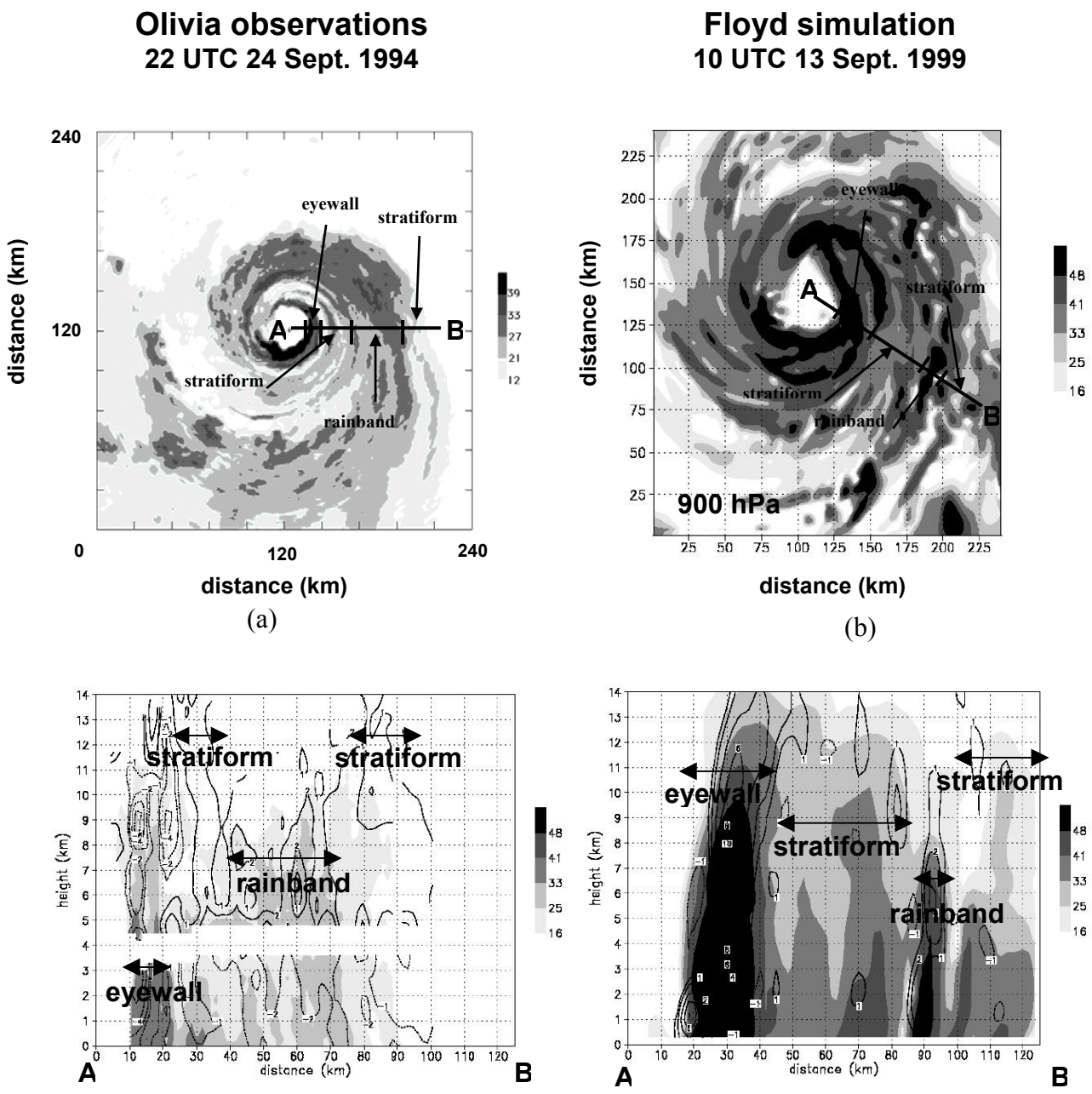

Figure 3. Examples of regime identification scheme for radar observations of Hurricane Olivia (1994) and simulation of Hurricane Floyd (1999). Plan view radar images are indicated in (a) and (b), radius-height cross sections are indicated in (c) and (d). Areas identified as eyewall, rainband, and stratiform are identified (note difference in scales of reflectivity between (a) and (b)).

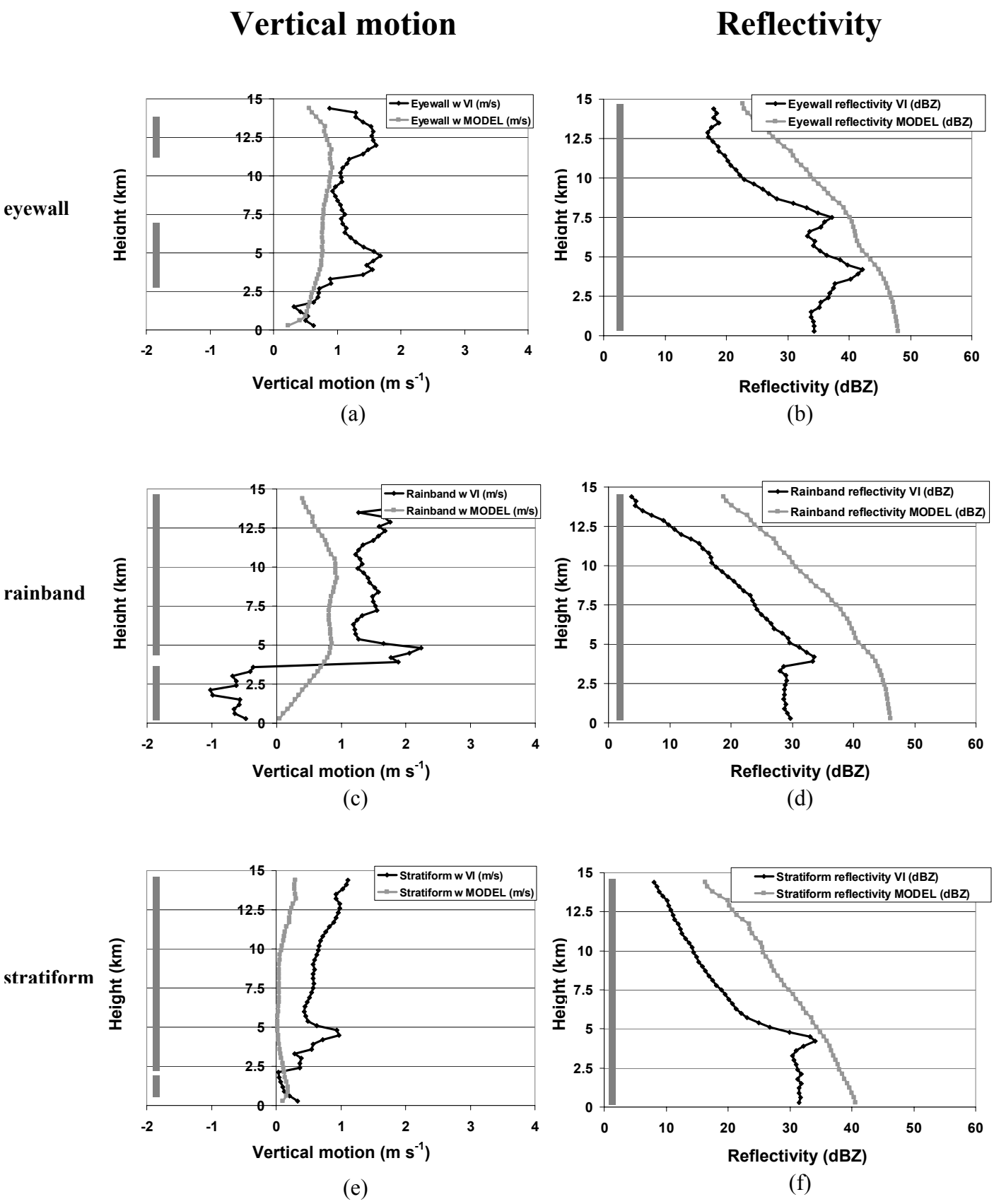

Figure 4. Profiles of Doppler-derived (a, c, and e) and simulated (b, d, and f) mean vertical motion (m s^{-1}) and reflectivity (dBZ) for all storms sorted by region. Vertical shaded bars denote those levels where differences are significant at the 99% confidence level.

Vertical motion

eyewall

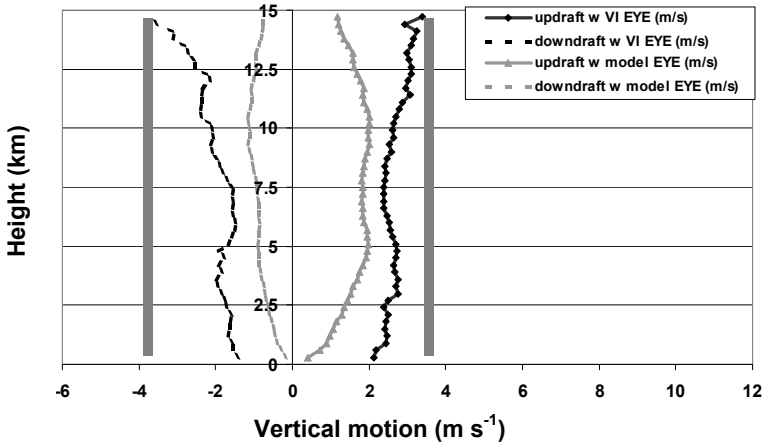

(a)

rainband

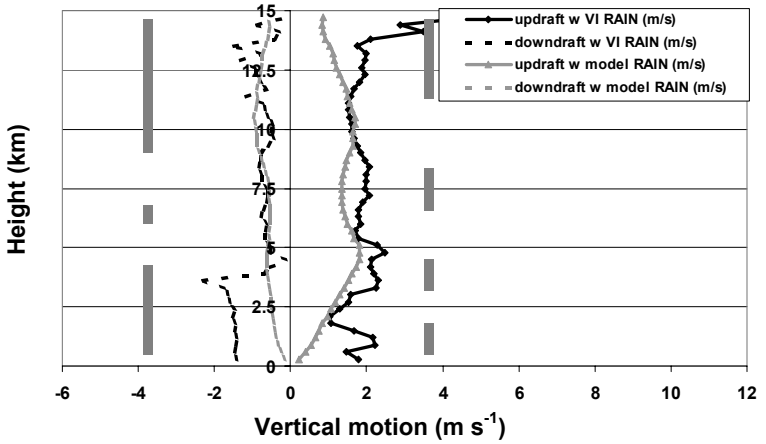

(b)

stratiform

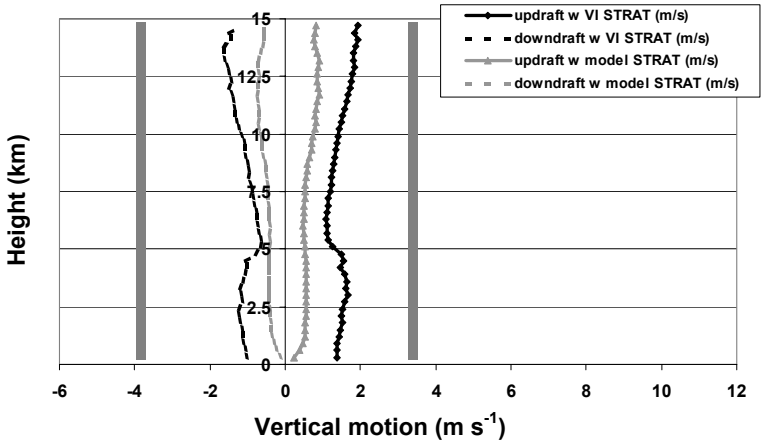

(c)

Figure 5. Profiles of observed and simulated mean updrafts and downdrafts (m s^{-1}) sorted by region. Vertical shaded bars denote those levels where differences are significant at the 99% confidence level.

Vertical motion

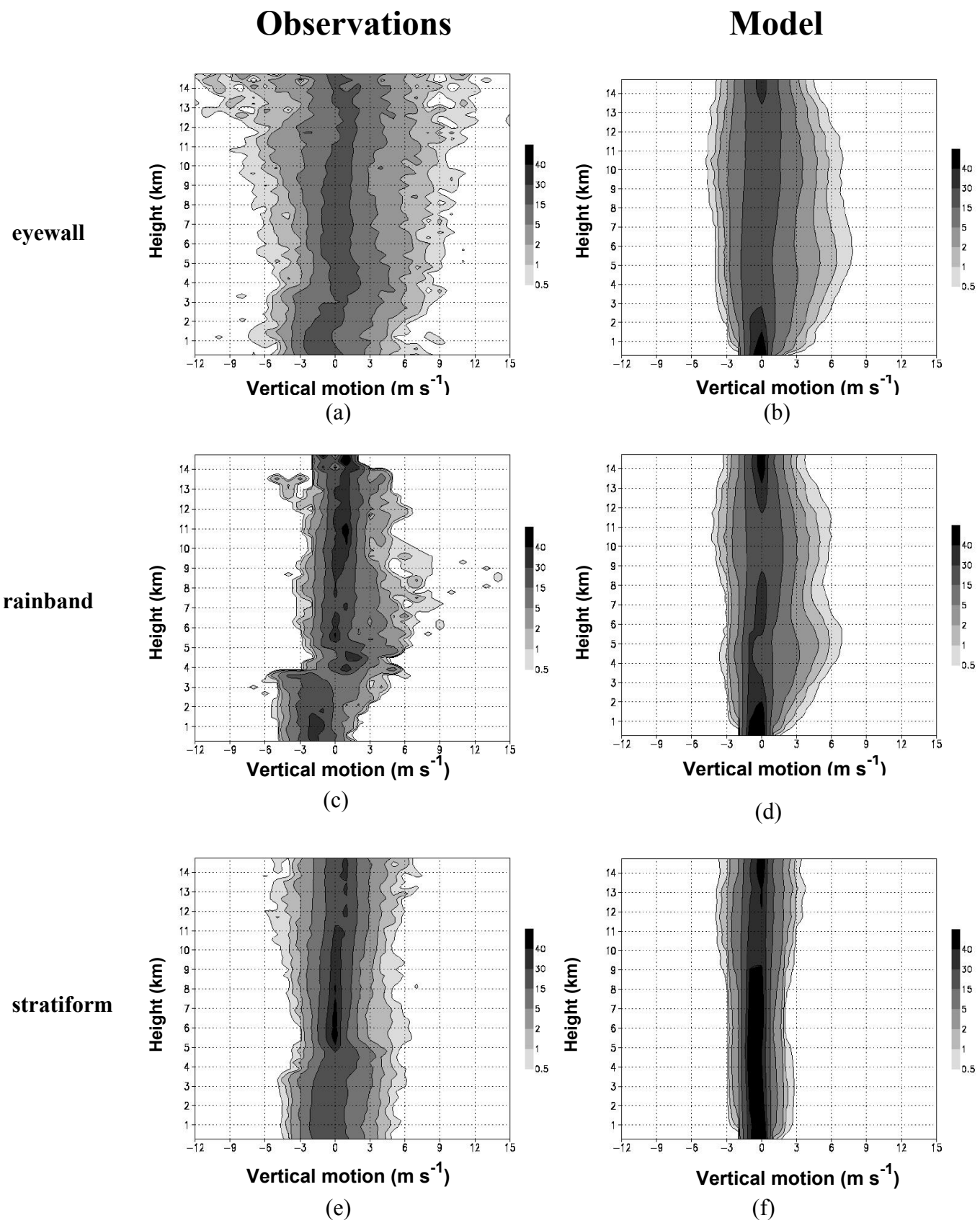

Figure 6. Contoured frequency by altitude diagrams (CFADs; shading, %) of Doppler-derived (a, c, and e) and simulated (b, d, and f) vertical motion for all storms sorted by region.

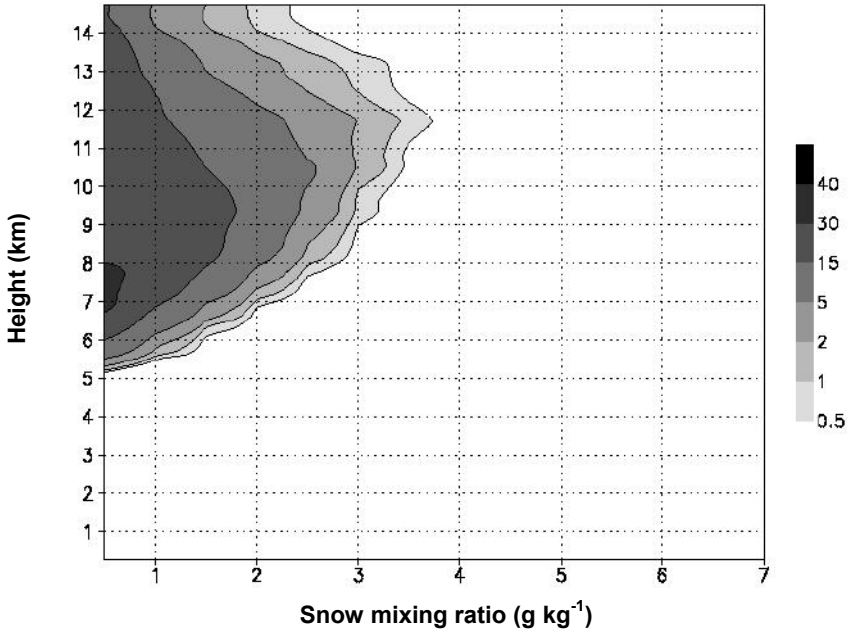

(a)

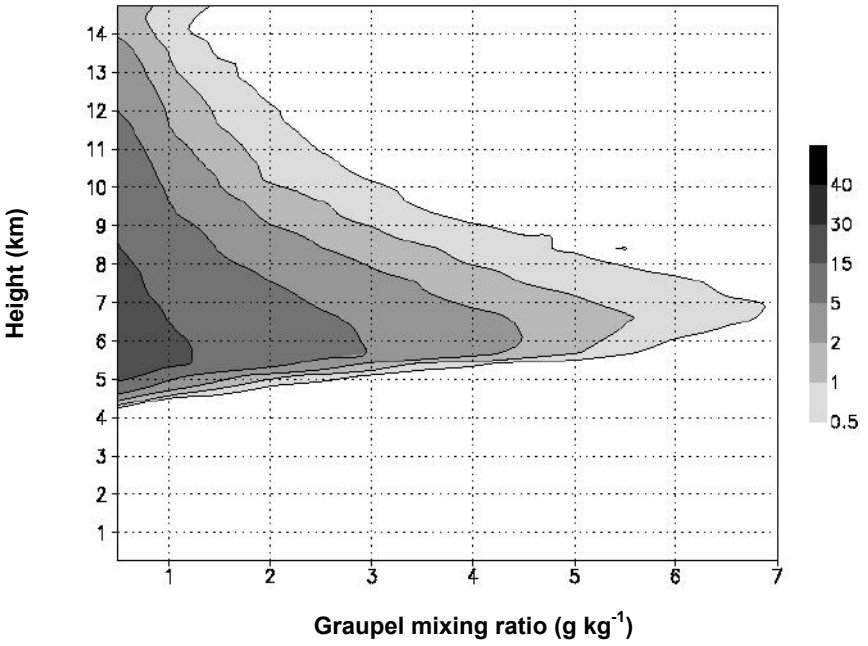

(b)

Figure 7. CFADs (shading, %) of simulated (a) snow mixing ratio and (b) graupel mixing ratio for the rainband region in the Bonnie and Floyd simulations.

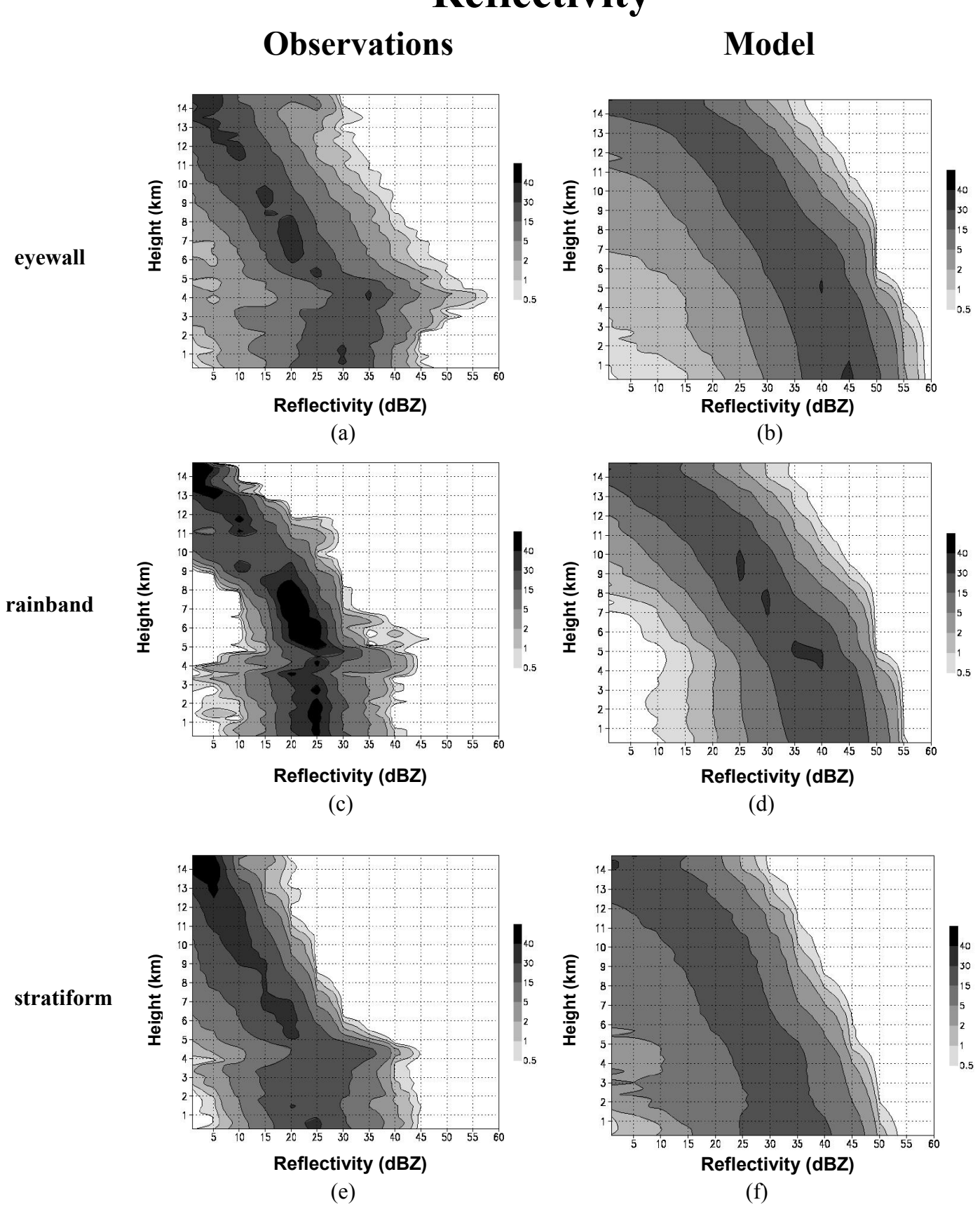

Figure 8. CFADs (shading, %) of reflectivity for all storms sorted by region.

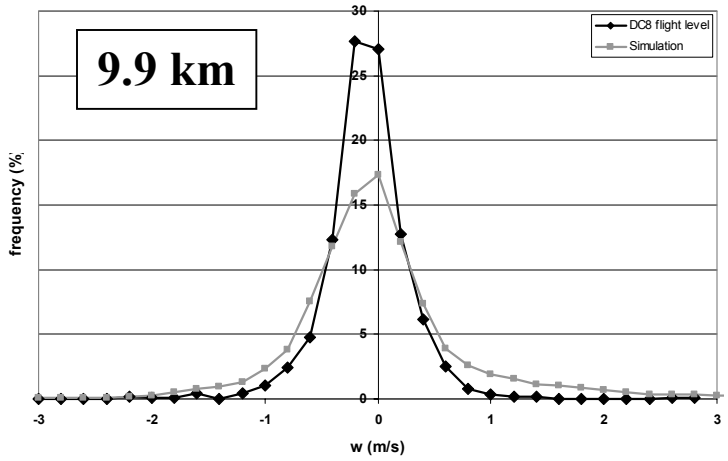

(a)

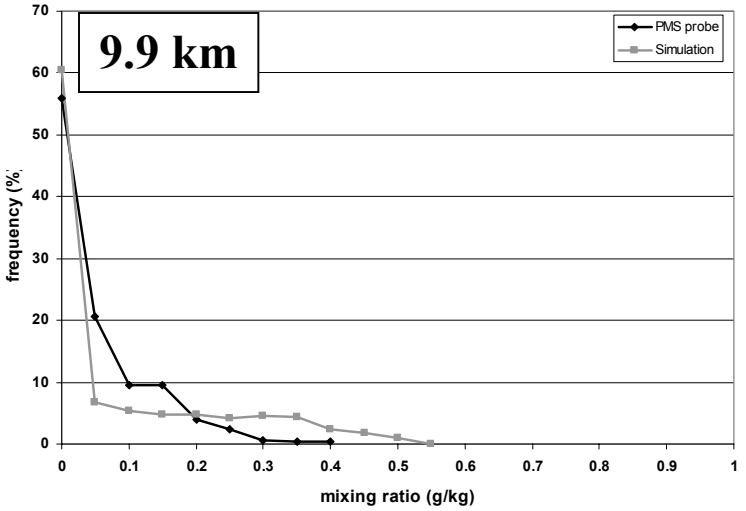

(b)

Figure 9. Probability distribution functions (PDFs; %) of (a) flight-level vertical motion and (b) hydrometeor mixing ratio at 9.9 km for observations and simulation of Bonnie.

Observations

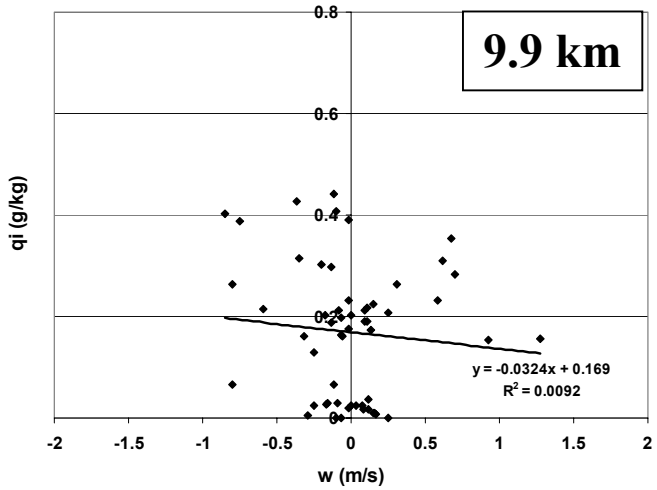

(a)

Model

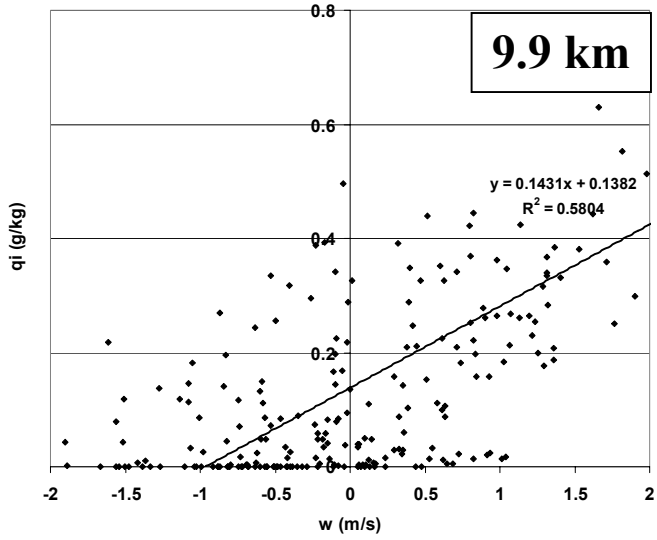

(b)

Figure 10. Scatter plots of flight-level vertical motion (m s^{-1}) and hydrometeor concentrations (g kg^{-1}) at 9.9 km for (a) observations and (b) simulation of Bonnie

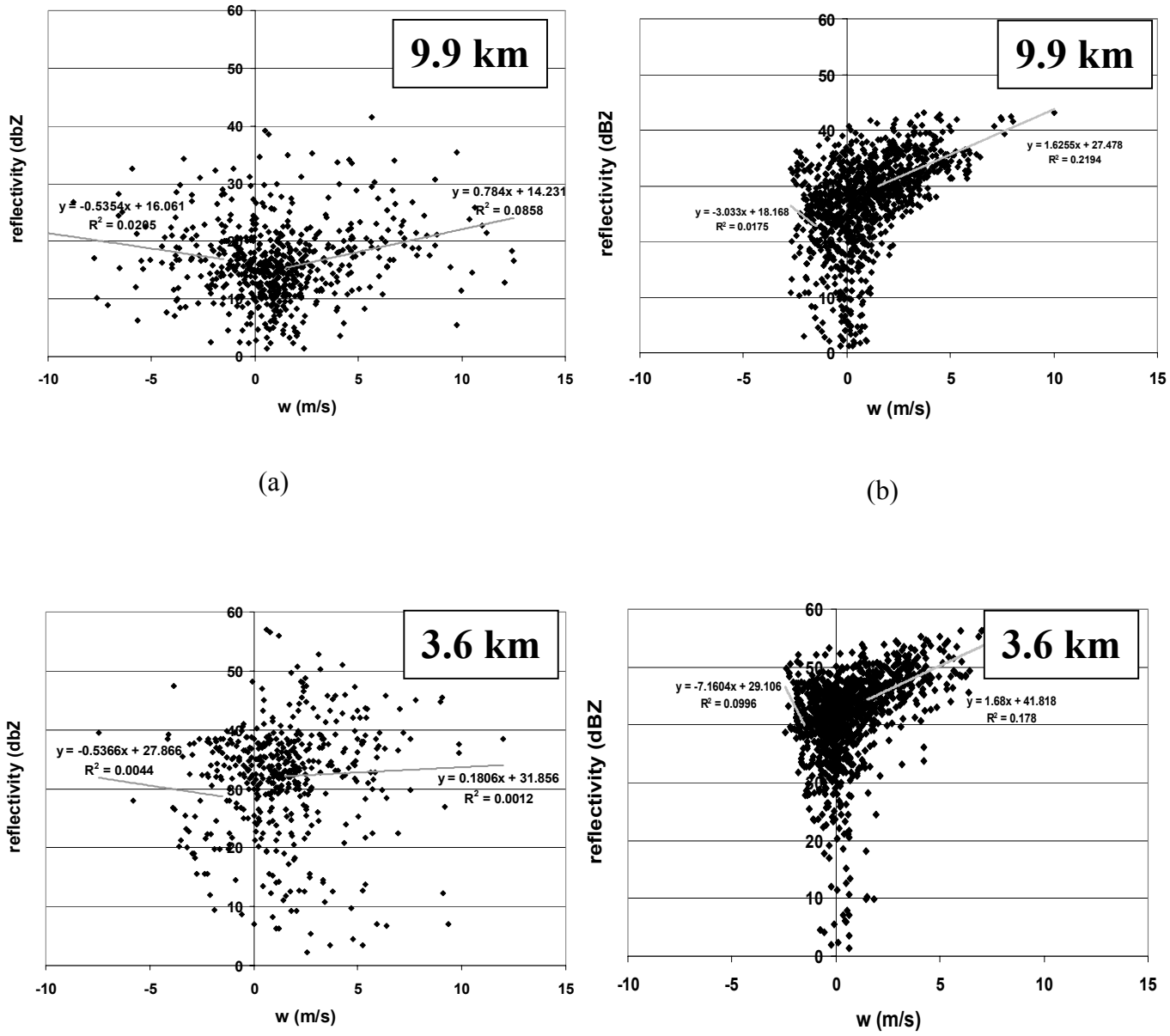

Figure 11. Scatter plots of Doppler-derived vertical motion (m s^{-1}) and reflectivity (dBZ) for all storms

observations

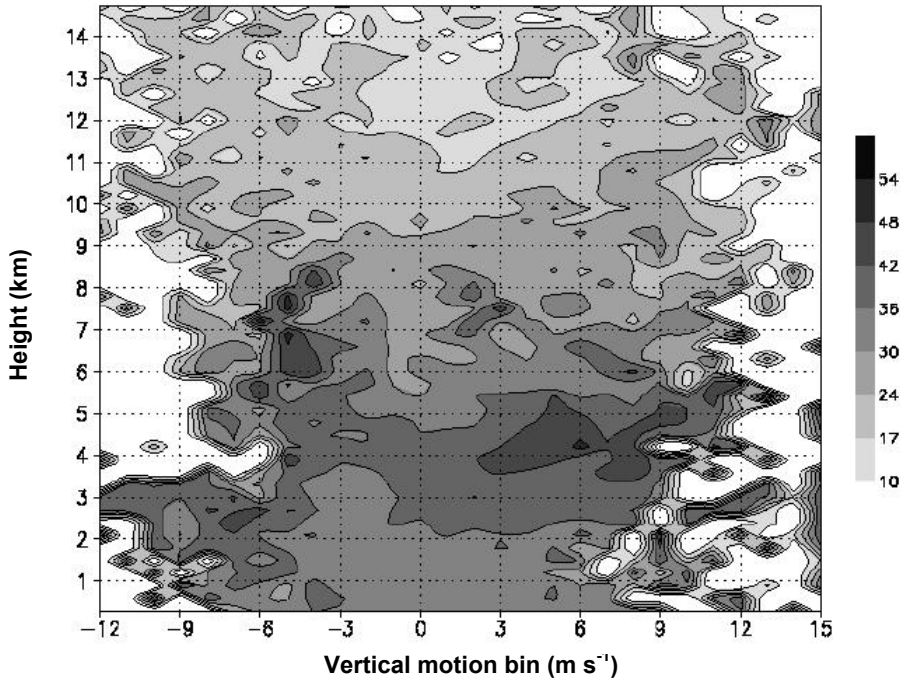

(a)

model

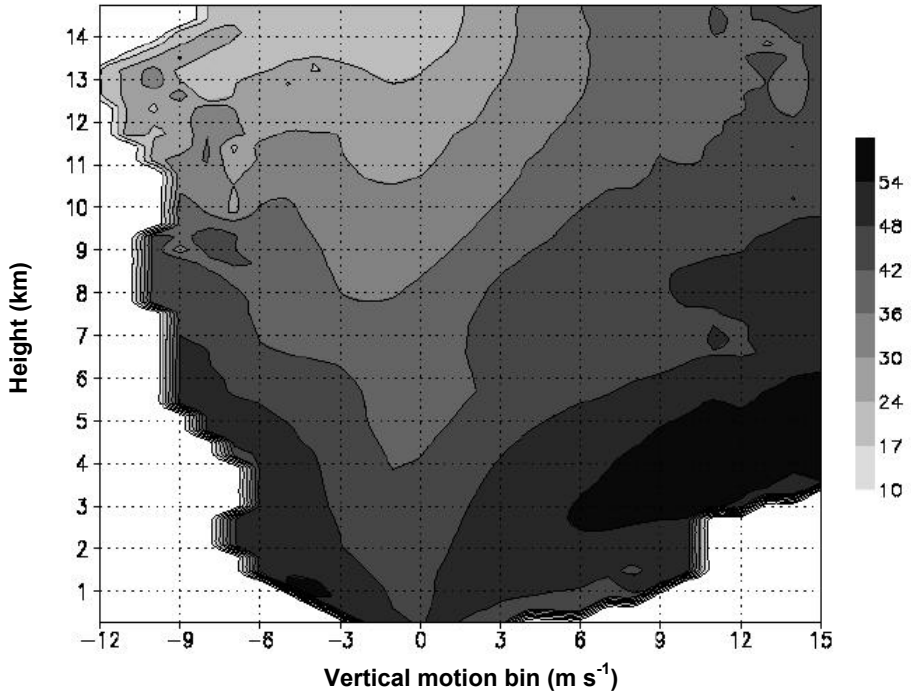

(b)

Figure 12. Mean eyewall reflectivity (shading, dbZ) stratified by Doppler-derived vertical motion bins for all storms.

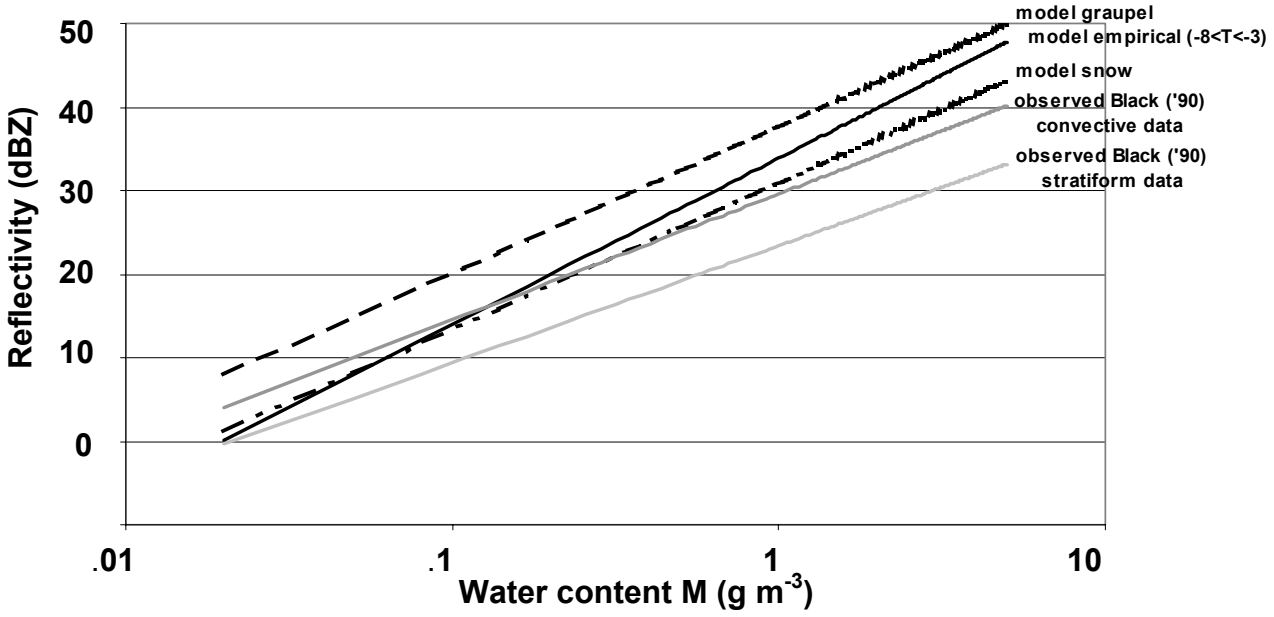

(a)

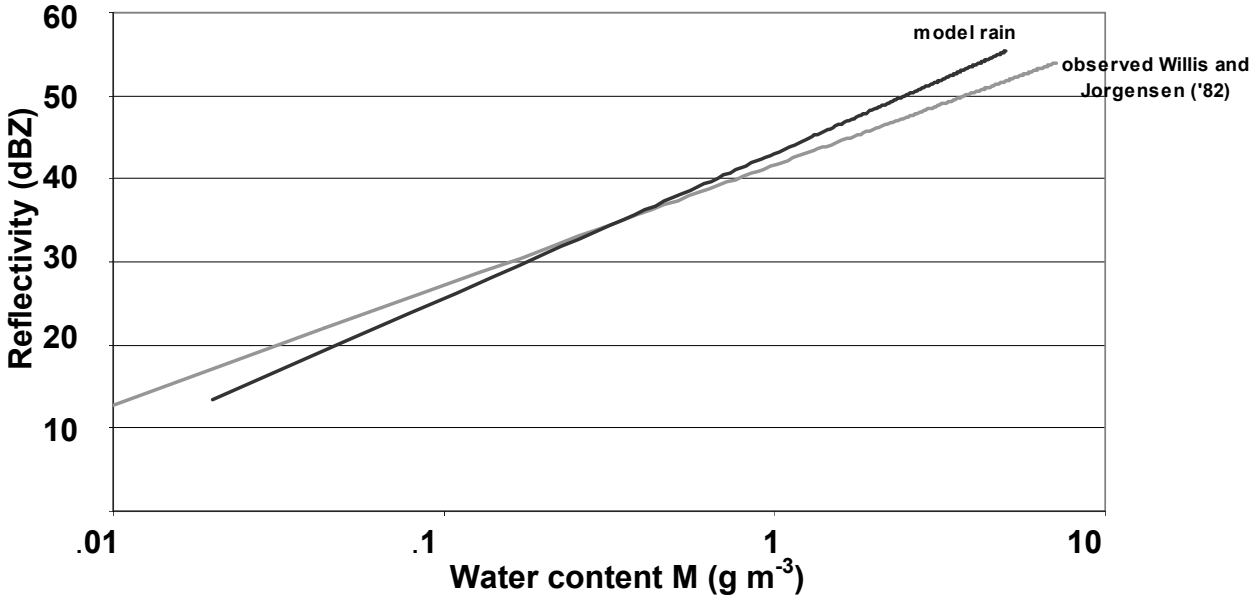

(b)

Figure 13. Comparisons of Z-M relations for (a) ice and (b) rain from simulations and from observed hurricane cases

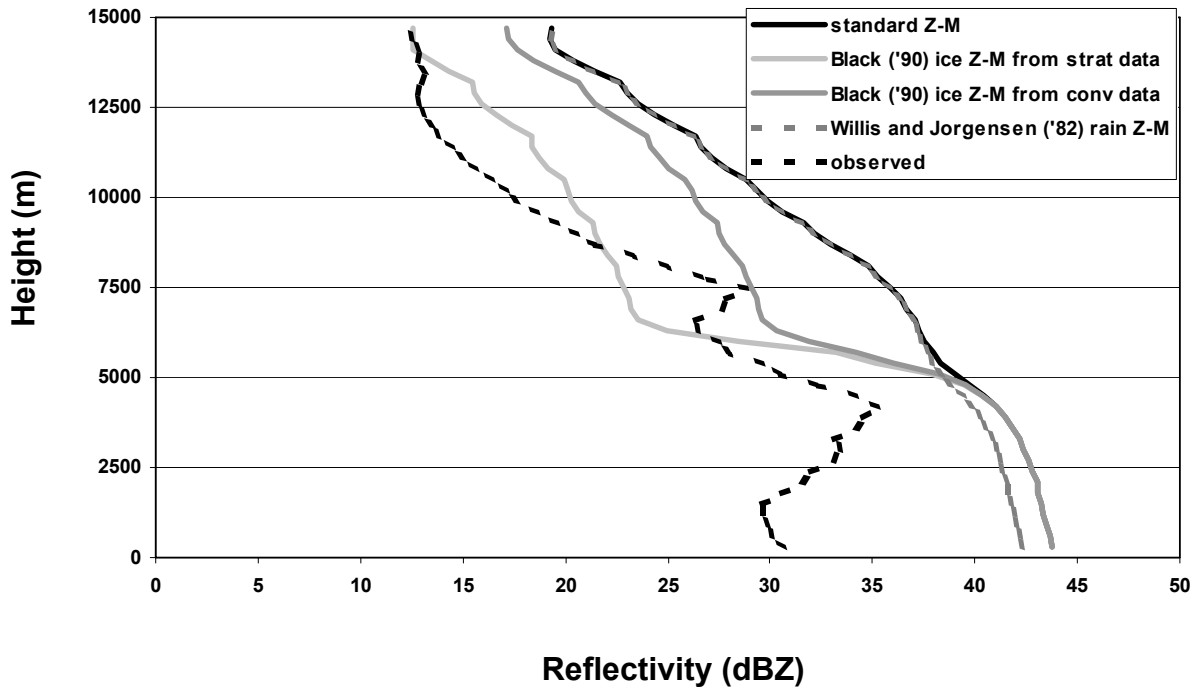

Figure 14. Profiles of mean reflectivity (dBZ) for all regions using different Z-M relations.

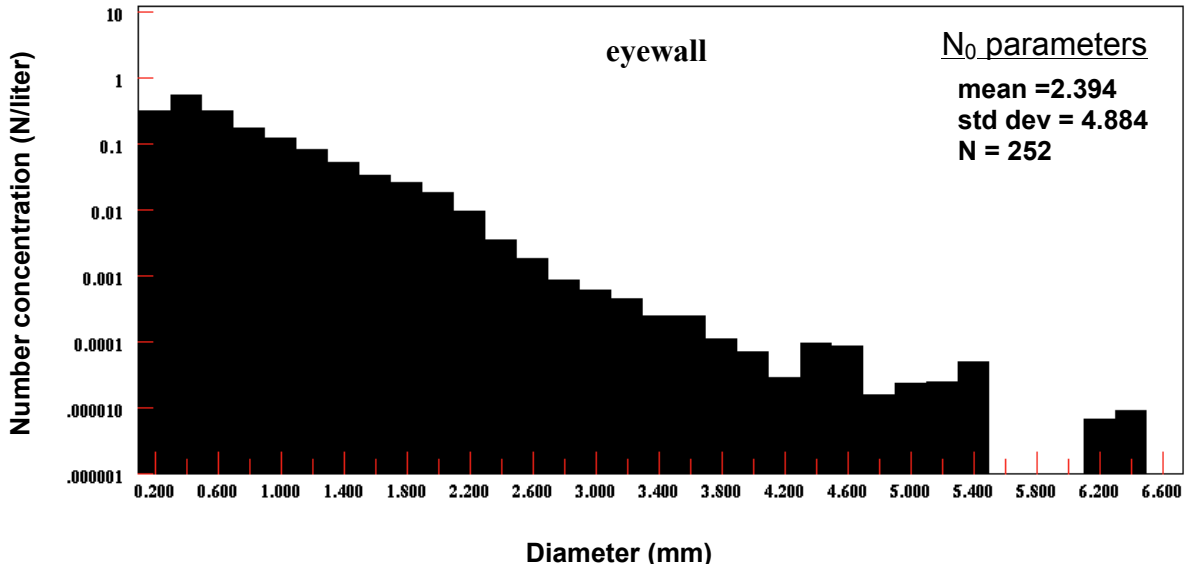

(a)

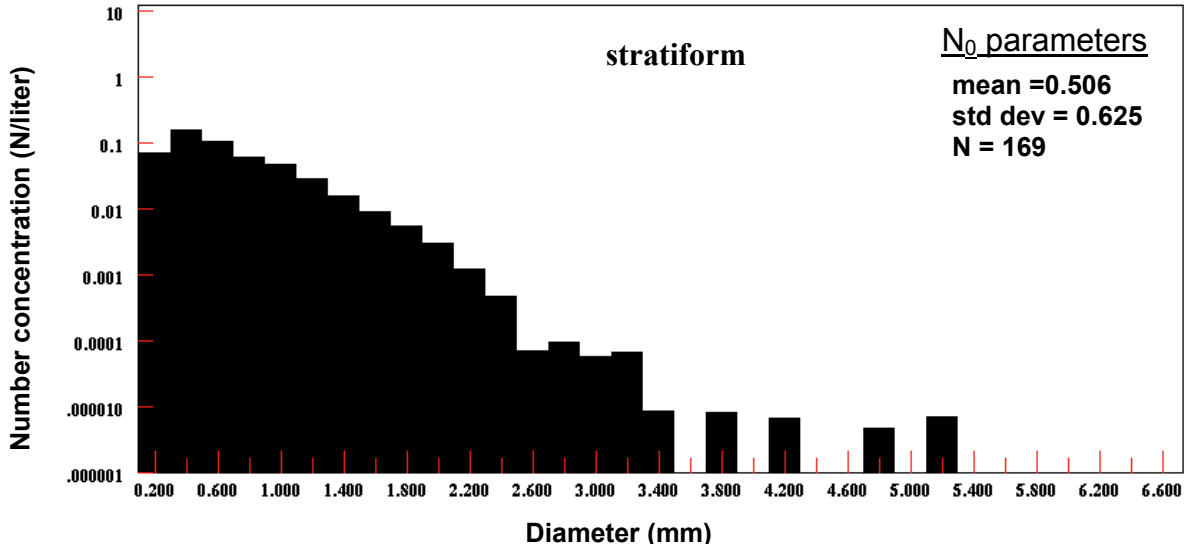

(b)

Figure 15. Average size distributions from 2D-P probe on P-3 aircraft from 22 September 1987 in Hurricane Emily (1987) for (a) eyewall regions and (b) stratiform regions. Altitude of aircraft was 4 km. Values of statistical parameters (mean, standard deviation, sample size) for intercept parameter calculated from each distribution shown in inset.

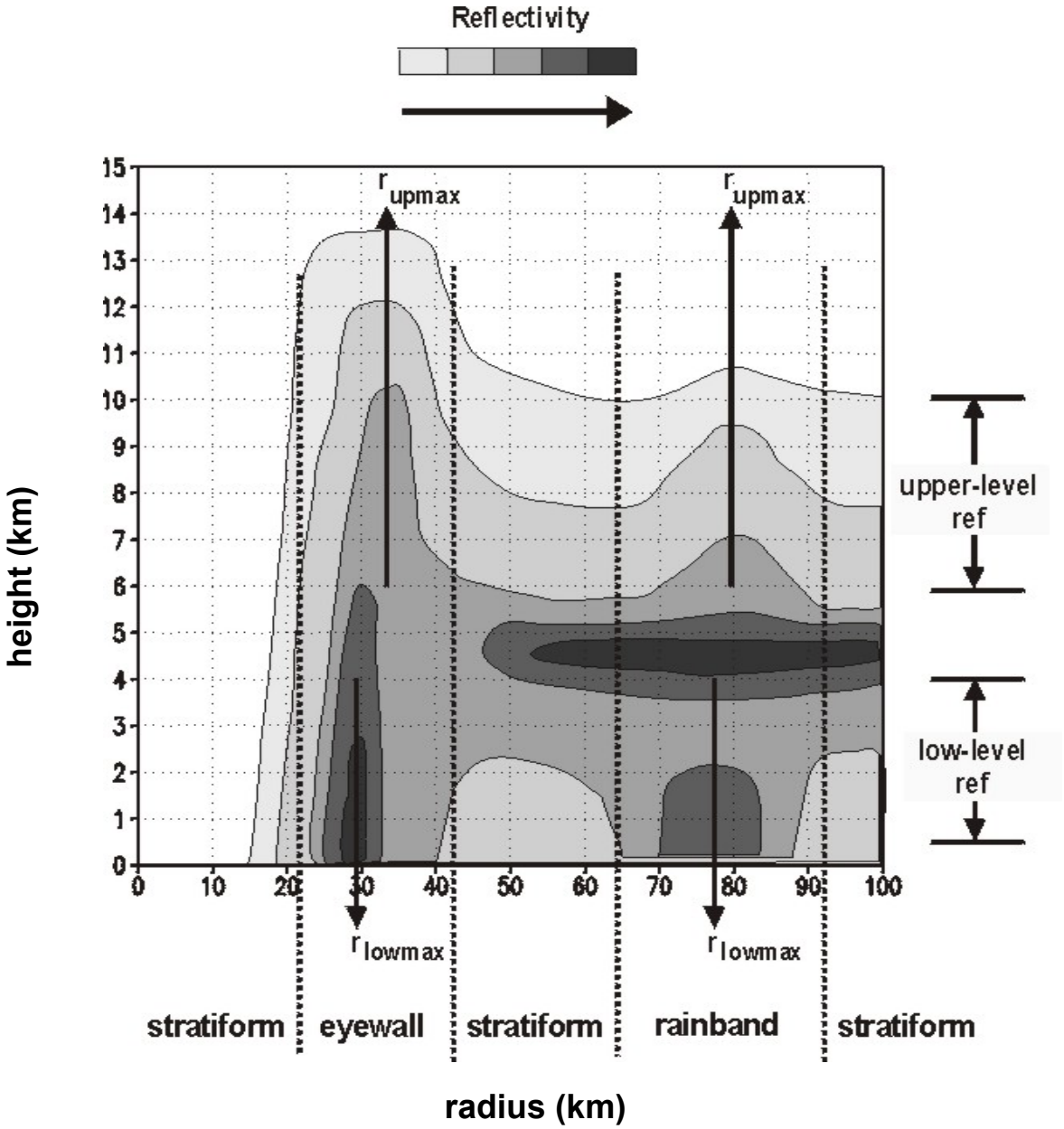

Figure A1. Schematic showing identification of candidate eyewall, rainband, and stratiform regions based on reflectivity.